Strong Evidence of Heterogeneous Processing on Stratospheric Sulfate Aerosol in the Extrapolar Southern Hemisphere Following the 2022 Hunga Tonga-Hunga Ha'apai Eruption

M. L. Santee[1], A. Lambert[1], L. Froidevaux[1], G. L. Manney[2,3], M. J. Schwartz[1], L. F. Millán[1], N. J. Livesey[1], W. G. Read[1], F. Werner[1], and R. A. Fuller[1]

[1]Jet Propulsion Laboratory, California Institute of Technology, Pasadena, CA, USA
[2]NorthWest Research Associates, Socorro, NM, USA
[3]New Mexico Institute of Mining and Technology, Socorro, NM, USA

Key Points:

- Satellite data show widespread stratospheric chlorine and nitrogen repartitioning in 2022 following the Hunga Tonga-Hunga Ha'apai eruption
- Observed composition changes are consistent with heterogeneous processing on volcanic sulfate aerosol, in particular the hydrolysis of N_2O_5
- Moderate enhancements in reactive chlorine in the southern mid- and low-latitude stratosphere did not cause appreciable chemical ozone loss

Corresponding author: M. L. Santee, `Michelle.L.Santee@jpl.nasa.gov`

Abstract

The January 2022 eruption of Hunga Tonga-Hunga Ha'apai (HT-HH) caused the largest enhancement in stratospheric aerosol loading in decades and produced an unprecedented enhancement in stratospheric water vapor, leading to strong stratospheric cooling that in turn induced changes in the large-scale circulation. Here we use satellite measurements of gas-phase constituents together with aerosol extinction to investigate the extent to which the thick aerosol, excess moisture, and strong cooling enabled heterogeneous chemical processing. In the southern tropics, unambiguous signatures of substantial chlorine and nitrogen repartitioning appear over a broad vertical domain almost immediately after the eruption, with depletion of N_2O_5, NO_x, and HCl accompanied by enhancement of HNO_3, ClO, and $ClONO_2$. After initially rising steeply, HNO_3 and ClO plateau, maintaining fairly constant abundances for several months. These patterns are consistent with the saturation of N_2O_5 hydrolysis, suggesting that this reaction is the primary mechanism for the observed composition changes. The southern midlatitudes and subtropics show similar but weaker enhancements in ClO and $ClONO_2$. In those regions, however, effects of anomalous transport dominate the evolution of HNO_3 and HCl, obscuring the signs of heterogeneous processing. Perturbations in chlorine species are considerably weaker than those measured in the southern midlatitude stratosphere in 2020 following the Australian New Year's fires. The moderate HT-HH-induced enhancements in reactive chlorine seen throughout the southern middle and low-latitude stratosphere, far smaller than those in typical winter polar vortices, do not lead to appreciable chemical ozone loss; rather, extrapolar lower-stratospheric ozone remains primarily controlled by dynamical processes.

Plain Language Summary

The January 2022 eruption of the Hunga Tonga-Hunga Ha'apai (HT-HH) volcano caused the largest increase in stratospheric aerosol in decades and produced an unprecedented increase in stratospheric water vapor, which led to strong stratospheric cooling that in turn altered stratospheric winds. Here we use satellite measurements to investigate the extent to which the thick aerosol, excess moisture, and strong cooling enabled heterogeneous chemical processing. In the southern tropics, unambiguous signatures of substantial changes in several chlorine and nitrogen species appear over a broad vertical range almost immediately after the eruption, with decreases in some species mirrored by increases in others. The southern midlatitudes and subtropics show similar but weaker evidence of chemical processing. In those regions, however, effects of anomalous wind patterns obscure the signs of heterogeneous processing in some species. Perturbations in chlorine are considerably weaker than those measured in the southern midlatitude stratosphere following the Australian New Year's fires in 2020. The moderate HT-HH-induced enhancements in reactive chlorine seen throughout the southern middle and low-latitude stratosphere, far smaller than those in typical winter polar vortices, do not lead to appreciable chemical ozone loss; rather, outside the polar regions, lower-stratospheric ozone remains primarily controlled by dynamical processes.

1 Introduction

The Hunga Tonga-Hunga Ha'apai (HT-HH) volcano in the Kingdom of Tonga began an eruptive sequence in December 2021 that culminated in a paroxysmal explosion on 15 January 2022 (e.g., Carn et al., 2022). It was the most explosive submarine eruption witnessed during the satellite era to date. Satellite and ground-based measurements indicate that a substantial amount of material was lofted into the upper stratosphere; although the bulk was deposited at altitudes between 20 and 30 km, the highest overshooting tops of the eruption column penetrated into the lower mesosphere, reaching an unprecedented ∼55 km altitude (Carr et al., 2022; Khaykin et al., 2022; Millán et al., 2022; Taha et al., 2022). The climactic blast was marked by the (previously undocumented

for a volcanic eruption) occurrence of a double umbrella cloud (that is, a cloud that spreads laterally around the level of neutral buoyancy and rapidly transports the ejected volume away from the volcano in all directions), with distinct signatures at about 30 km and near the tropopause at ∼17 km (Gupta et al., 2022). Also unprecedented was the mass of water vapor injected by HT-HH into the stratosphere, which has been estimated using Microwave Limb Sounder measurements to have increased the total stratospheric water vapor burden by ∼10% (Millán et al., 2022); other studies have calculated similar values for the magnitude of the water vapor injection (Khaykin et al., 2022; Vömel et al., 2022; Xu et al., 2022). Analysis of its isotopic composition shows that the injected water derived mainly from vaporized seawater, although some tropospheric moisture may also have been entrained by the eruptive updraft (Khaykin et al., 2022). Peak enhancements in water vapor were observed in the 25–30 km region (Khaykin et al., 2022; Millán et al., 2022; Sellitto et al., 2022; Vömel et al., 2022; Xu et al., 2022), consistent with being sourced from the upper umbrella cloud (Gupta et al., 2022). The eruption column was also rich in ice (Gupta et al., 2022; Khaykin et al., 2022); subsequent sedimentation and sublimation of ice led to relatively humid conditions in the lower stratosphere (Khaykin et al., 2022; Millán et al., 2022).

Although the explosive energy of HT-HH was similar to or even larger than that of the 1991 eruption of Mt. Pinatubo (Poli & Shapiro, 2022; Wright et al., 2022; Yuen et al., 2022), its SO_2 discharge into the stratosphere was ∼1–2 orders of magnitude smaller (Carn et al., 2022; Millán et al., 2022; Sellitto et al., 2022). SO_2 emissions from submarine volcanoes are typically lower than those from non-hydromagmatic eruptions of comparable magnitude, presumably because of significant scrubbing of SO_2 in their water-rich eruption clouds (Carn et al., 2022). In addition, the SO_2 from HT-HH that did enter the stratosphere had a considerably shortened lifetime, undergoing unusually rapid conversion to secondary sulfate aerosol (Legras et al., 2022; Sellitto et al., 2022). The exceptionally fast formation of sulfate aerosol is also attributable to the abundant co-emitted water vapor, which provides a source of OH that in turn catalyzes the oxidation of SO_2 into H_2SO_4, which then nucleates into sulfate aerosol (Zhu et al., 2022). With its modest SO_2 emissions, HT-HH caused global-mean anomalies in stratospheric aerosol optical depth smaller by about a factor of 6 than those resulting from Pinatubo (Khaykin et al., 2022; Sellitto et al., 2022). Nevertheless, HT-HH led to the largest perturbation in the stratospheric aerosol loading in the last 30 years (Khaykin et al., 2022; Sellitto et al., 2022; Taha et al., 2022).

For the first few months after the eruption, the main volcanic cloud at 20–30 km remained largely confined within the tropical pipe as it encircled the globe; thereafter it gradually dispersed meridionally, with more efficient transport in the Southern Hemisphere, such that by June 2022 it had spread from about 60°S to 30°N, with small fragments reaching higher northern latitudes (Coy et al., 2022; Legras et al., 2022; Millán et al., 2022; Schoeberl et al., 2022, 2023; Taha et al., 2022). The strong transport barrier at the boundary of the Antarctic vortex prevented the plume from penetrating to high southern latitudes until that vortex broke down in late 2022 (Manney et al., 2023). Initially the enhanced aerosol and water vapor were spatially coincident, but they gradually diverged. Entrained within the ascending branch of the Brewer-Dobson circulation, the moisture anomaly was carried upward in the months following its injection, whereas the sulfate aerosols were subject to gravitational settling; hence the aerosol- and water-rich layers became increasingly separated in the vertical after mid-February (Legras et al., 2022; Schoeberl et al., 2022).

Both the aerosol and the water vapor perturbations induced radiative effects, but infrared cooling from enhanced water vapor concentrations was shown to dominate (Legras et al., 2022; Sellitto et al., 2022; Jenkins et al., 2023), leading to the development of a strong and persistent low-temperature anomaly in the mid-stratosphere shortly after the eruption (Coy et al., 2022; Schoeberl et al., 2022; Vömel et al., 2022). The anomalous

temperature structure in turn induced changes in the large-scale circulation; in particular, zonal winds in the mid-stratosphere strengthened, as did meridional flow, while descent in the middle and high latitudes slowed (Coy et al., 2022).

Enhanced sulfate aerosol loading following volcanic injection of SO_2 into the stratosphere is known to perturb the partitioning of key chemical families controlling stratospheric ozone (e.g., Solomon, 1999). The exceptional stratospheric hydration and ensuing temperature anomalies caused by HT-HH may have increased such chemical processing. Transport also plays a major role in shaping trace gas distributions, however, and the alterations to the stratospheric circulation arising from the eruption may have either compounded or attenuated the chemical effects, complicating interpretation of observed changes in composition. Here we investigate the impact of the HT-HH eruption on stratospheric composition using satellite measurements.

2 Data and Methods

We examine measurements of H_2O, HNO_3, ClO, HCl, N_2O, and O_3 from the Aura Microwave Limb Sounder (MLS) (e.g., Waters et al., 2006). The enormous enhancement in stratospheric water vapor from HT-HH, with the largest concentrations more than an order of magnitude greater than any previously observed by MLS, degraded the accuracy of some of the products retrieved using the most recent MLS data processing algorithms, version 5 (v5). It also caused a large proportion of the measurements in the plume to fail the recommended MLS quality screening for the first few weeks after the eruption, with retrieval performance not returning to normal until 8 February 2022. For these reasons, Millán et al. (2022) used v4 MLS data to study the early stages of HT-HH plume evolution; moreover, they did not impose quality filtering on the data. Since v5 generally represents an improvement over v4, particularly for H_2O and N_2O, and since our main focus here is on the perturbations in composition arising in the weeks to months following the eruption, we use v5 MLS data for all species, with standard data screening protocols applied (Livesey et al., 2020).

MLS v5 ClO suffers from non-negligible biases at the lowest retrieval levels, 68–147 hPa (Livesey et al., 2020). As no substantial enhancement in nighttime ClO is expected in the extrapolar regions of interest here, the ClO biases are mitigated by taking ascending (∼2–3 PM at these latitudes) minus descending (∼2–3 AM) differences, similar to the strategy adopted in a prior study of midlatitude chlorine partitioning by Santee et al. (2022). MLS N_2O is subject to a negative drift that, while partially alleviated in v5, remains about −3%/decade in the lower stratosphere (Livesey et al., 2021). Accordingly, the MLS N_2O fields presented below have been "detrended" by removing a linear fit to the daily values across the Aura mission at each gridpoint.

We use meteorological fields (temperature, potential temperature, potential vorticity (PV)) from the Modern Era Retrospective Analysis for Research and Applications Version 2 (MERRA-2, Gelaro et al., 2017). Satellite data are cast into quasi-Lagrangian PV-based equivalent latitude (EqL) (Butchart & Remsberg, 1986) and potential temperature coordinates to facilitate tracking stratospheric air motions and allow parcels with similar dynamical histories to be grouped together. Each day on average ∼330 MLS profiles fall within each of the 16° EqL bands defined here: 38°S–54°S EqL, 22°S–38°S EqL, and 6°S–22°S EqL, representing southern midlatitudes, subtropics, and tropics, respectively.

In addition to MLS data, we use version 4.1/4.2 measurements of N_2O_5, NO, NO_2, and $ClONO_2$ from the Atmospheric Chemistry Experiment-Fourier Transform Spectrometer (ACE-FTS; Boone et al., 2020), screened using the recommended quality flags (Sheese et al., 2015; Sheese & Walker, 2020). In conjunction with the trace gas measurements, we use the latest version (V2.1) aerosol extinction coefficient profiles obtained by the Suomi-

NPP Ozone Mapping and Profiler Suite Limb Profiler (OMPS-LP) at both 869 nm, as recommended for tracking stratospheric injections from events such as volcanic eruptions or wildfires (Taha et al., 2021), and 745 nm. According to Taha et al. (2022), the standard V2.1 OMPS-LP algorithms provide accurate aerosol retrievals as long as the volcanic cloud is below 36 km; our analysis here is confined to the region below ∼33 km (900 K). We also compared the NASA OMPS-LP V2.1 aerosol products with the tomographic retrievals at 745 nm produced by the University of Saskatchewan (USask v1.2; Bourassa et al., 2023). Although the NASA and USask aerosol products show substantial differences at low latitudes below 500 K, those discrepancies have no bearing on our conclusions, and for simplicity only the NASA aerosol data at 869 nm are shown here. As in the study by Santee et al. (2022), for interpolation to isentropic surfaces, the aerosol data are first converted to cross section per mole of air (in units of $m^2\,mol^{-1}$), which, unlike the more commonly used extinction coefficient (in units of km^{-1}), is conserved under changes of atmospheric pressure in the absence of aerosol formation or loss. The conversion factor relating cross section to extinction is the local molar volume, RT/p (in units of $m^3\,mol^{-1}$), where R is the molar gas constant, T is temperature, and p is pressure. We use the remotely sensed optical properties without conversion to aerosol surface area or volume density, as would be necessary to use these data as inputs in chemical models (e.g., Hervig & Deshler, 1998; Kovilakam & Deshler, 2015).

3 Aerosol-Mediated Chemical Repartitioning

Within a few weeks of an explosive volcanic eruption, oxidative processing of the SO_2 injected into the stratosphere leads to the production of liquid sulfate particles, enhancing the aerosol surface area density (SAD) available for heterogeneous chemical processing (e.g., Bekki & Pyle, 1994). Heterogeneous reactions of particular importance in the stratosphere include (e.g., Solomon, 1999):

$$N_2O_5 + H_2O \rightarrow 2\,HNO_3 \quad \text{(R1)}$$
$$ClONO_2 + H_2O \rightarrow HOCl + HNO_3 \quad \text{(R2)}$$
$$ClONO_2 + HCl \rightarrow Cl_2 + HNO_3 \quad \text{(R3)}$$
$$HOCl + HCl \rightarrow Cl_2 + H_2O \quad \text{(R4)}$$
$$BrONO_2 + H_2O \rightarrow HOBr + HNO_3 \quad \text{(R5)}$$

Nitrogen, chlorine, and hydrogen photochemistry are strongly coupled, thus changes in the partitioning of one chemical family affect species in other families. Substantial perturbations in chemical partitioning can persist, as it can take a year or more for volcanic sulfate aerosols to be removed from the stratosphere through sedimentation. To set the stage for the interpretation of satellite measurements in Section 4, we first summarize the expected impacts of R1–R5 on several key nitrogen and chlorine species affecting stratospheric ozone, as well as ozone itself, under volcanically enhanced aerosol conditions. The chemical processes discussed here are described in greater detail by, for example, Bekki and Pyle (1994), Kinnison et al. (1994), Tie et al. (1994), Coffey (1996), Solomon (1999), Anderson et al. (2012), Berthet et al. (2017), and Robrecht et al. (2019). For brevity, these references are not cited for all relevant points in the following text.

3.1 HNO_3, N_2O_5, and NO_x

HNO_3 is the major reservoir for odd nitrogen, NO_y, in the lower stratosphere. In the immediate aftermath of the HT-HH eruption, a few individual MLS profiles showed strong stratospheric enrichments in several trace gases, including HNO_3 (Millán et al., 2022, their Figure S1). Although it has been measured in volcanic plumes near the ground (e.g., Mather et al., 2004; Oppenheimer et al., 2010; Voigt et al., 2014), in the lower strato-

sphere volcanogenic HNO_3 has been conclusively detected only once, when a peak mixing ratio of ∼3 ppbv above background was measured in an encounter with the fresh volcanic cloud from the February 2000 eruption of Hekla (Hunton et al., 2005; Rose et al., 2006). Major explosive eruptions can enhance stratospheric HNO_3 through injection, either of HNO_3 itself or of nitrogen-bearing gases (e.g., ammonia) from which it can be generated. Volcanic lightning can also induce HNO_3 formation, and, in addition to its other unprecedented characteristics, HT-HH produced prodigious amounts of lightning (Yuen et al., 2022). Thus, a direct volcanic origin for the anomalous post-eruption MLS HNO_3 profiles is possible. However, they are more likely to be retrieval artifacts arising from contamination of the MLS HNO_3 spectral signature by SO_2. In any case, these few highly localized and transient HNO_3 enhancements do not significantly affect the broad EqL-band averages analyzed in this study, and they are not considered further.

Hydrolysis of N_2O_5 (R1) is fairly insensitive to temperature (Figure S1 in Supporting Information) and takes place rapidly under virtually all stratospheric conditions. Its rate is intensified dramatically when a major volcanic eruption enhances aerosol SAD. Since (i) N_2O_5 is the main nighttime reservoir for reactive nitrogen, NO_x (defined here as NO+NO_2), (ii) the HNO_3 produced through R1 returns to the gas phase, and (iii) the rate at which HNO_3 undergoes conversion back to NO_x is unchanged, an increase in SAD is generally expected to be accompanied by observed decreases in the abundances of both N_2O_5 and NO_x and a corresponding increase in HNO_3. Similarly, R5 (hydrolysis of $BrONO_2$) can be active at all latitudes and seasons during periods of high aerosol loading.

$ClONO_2$ hydrolysis (R2) and reaction with HCl (R3) on sulfate aerosol are also potential sinks of NO_x and sources of gas-phase HNO_3. Unlike for R1 and R5, the reaction probabilities of R2 and R3 are strongly dependent on particle water content and hence temperature (Figure S1 in Supporting Information), and typically they only become competitive with R1 in affecting nitrogen (and chlorine) partitioning under cold (T<∼200 K) conditions, such as in the winter polar regions, where they take place on the surfaces of polar stratospheric cloud (PSC) particles. These two reactions, however, can come into play to convert NO_x to HNO_3 in the midlatitude lower stratosphere when SAD and water vapor mixing ratios (and hence the aerosol water fraction) are sufficiently elevated (Keim et al., 1996). Whereas condensed HNO_3 remains sequestered in PSCs in the winter polar regions, at higher temperatures a large proportion of the HNO_3 formed by these reactions is released to the gas phase (Robrecht et al., 2019).

Consistent with heterogeneous processing, substantial reductions in NO_x and/or N_2O_5 have been seen following several large eruptions (e.g., Fahey et al., 1993; Mills et al., 1993; Koike et al., 1994; Rinsland et al., 1994; Coffey, 1996; Adams et al., 2017; Berthet et al., 2017; Zambri et al., 2019). Significant decreases in NO_x observed in the months after severe wildfires in Australia in the austral summer of 2019/2020 have also pointed to the occurrence of heterogeneous processing on smoke particle surfaces (Solomon et al., 2022; Strahan et al., 2022). Observational evidence for associated increases in HNO_3 has been more ambiguous, however. Strongly enhanced HNO_3 (as high as 40–50% above unperturbed background values in some cases) was measured in aged stratospheric volcanic clouds sampled weeks or months after major eruptions (Arnold et al., 1990; Koike et al., 1994; Rinsland et al., 1994; Jurkat et al., 2010). In addition, declining trends in HNO_3 abundances as the sulfate aerosol loading from the eruption of Mt. Pinatubo slowly decayed in subsequent years were attributed to the diminishing impact of R1 (David et al., 1994; Kumer et al., 1996; Slusser et al., 1998; Rinsland et al., 2003; Santee et al., 2004). In other cases, by contrast, no clear volcanic enhancement in HNO_3 was seen (Coffey, 1996; Adams et al., 2017; Berthet et al., 2017). Nor were HNO_3 abundances elevated following the 2019/2020 Australian fires (Santee et al., 2022; Strahan et al., 2022).

Zambri et al. (2019) used coupled chemistry-climate model simulations in conjunction with MLS and other satellite measurements to investigate the impact on stratospheric composition of multiple moderate-magnitude eruptions in the post-Pinatubo era. Neg-

ative anomalies (with respect to unperturbed background values) in response to eruptive events were seen in modeled N_2O_5 and measured and modeled NO_x, particularly at 50–70 hPa, where anomalies exceeded 20–25%. The model showed a clear relationship between SAD and HNO_3 changes through much of the stratosphere, but the perturbations in HNO_3 were not entirely congruent with those in NO_x. In particular, positive anomalies in HNO_3 extended over a larger altitude range, exceeding 10% during periods of increased sulfate aerosol SAD at levels from 70 to 5 hPa, with the exception of 50 hPa, where fractional changes were much smaller than those in NO_x and confined mainly to the tropics. MLS data indicated similar, albeit weaker, aerosol-induced HNO_3 increases, again except near 50 hPa. Zambri et al. (2019) offered no explanation for the behavior seen in both measured and modeled HNO_3 fields at 50 hPa. Other recent modeling studies have also found post-eruption reductions in NO_x and N_2O_5 of as much as 25–50% but concomitant increases in HNO_3 of only 5–15% (Adams et al., 2017; Berthet et al., 2017).

It may not be surprising that a strong correlation between SAD/NO_x and HNO_3 is not consistently observed; HNO_3 concentrations in the lower stratosphere are much larger than those of NO_x, and thus comparable changes in its abundance have only modest relative effects. Small changes are difficult to detect against the backdrop of natural dynamical variability, which is of order 10% for HNO_3 in the lower stratosphere, making HNO_3 a less sensitive indicator of the occurrence of R1 than NO_x (e.g., Adams et al., 2017; Solomon et al., 2022; Strahan et al., 2022).

3.2 ClO

ClO is the main form of ozone-destroying reactive chlorine. In the week following the HT-HH eruption, MLS recorded strongly enhanced ClO in a handful of profiles (Millán et al., 2022). The only halogenated compounds known to have been volcanically injected into the stratosphere are HCl (discussed in Section 3.3) and OClO (Theys et al., 2014), and the measured high ClO values were thought to largely reflect MLS retrieval artifacts arising from SO_2 spectral interference, rather than direct stratospheric injection of ClO. Given its rapid transformation into sulfate aerosol, the SO_2 from HT-HH no longer compromised the reliability of MLS retrievals after late January, when abundances reverted to background levels (Millán et al., 2022). As we are concerned here with the signatures of spatially extensive chemical processing that manifest weeks to months after the HT-HH injection, the initial enhancements in a few ClO profiles are not considered further.

Post-eruption decreases in NO_x impede $ClONO_2$ formation, shifting chlorine partitioning toward ClO. These gas-phase processes affect ClO and $ClONO_2$ abundances while leaving HCl unchanged. In addition, photolysis of the gas-phase HNO_3 and HOBr resulting from the hydrolysis of N_2O_5, $ClONO_2$, and $BrONO_2$ (R1, R2, and R5) is a source of reactive hydrogen, HO_x ($OH+HO_2$), and reduced NO_x concentrations also bring about increases in HO_x by inhibiting the rate of $NO_2+OH+M \rightarrow HNO_3+M$. In the case of HT-HH, moreover, simulations show that the massive injection of water vapor rapidly increased stratospheric OH abundances (Zhu et al., 2022). Elevated OH abundances in turn accelerate conversion of HCl to reactive chlorine via $HCl+OH \rightarrow Cl+H_2O$. Thus, small enhancements in stratospheric ClO may occur following major volcanic eruptions from R1 and R5 alone, under conditions unfavorable for R2–R4 (which may also occur on volcanic sulfate aerosol where ambient temperatures and water vapor abundances allow). Although in general the consequences of increased OH on stratospheric chlorine partitioning are expected to be relatively minor, in the extremely water-rich environment after HT-HH, the gas-phase oxidation of HCl may be intensified.

Enhancements in ClO of a few tens to 100 ppt observed outside of the polar regions in the months following the eruption of Mt. Pinatubo were attributed to heterogeneous processing on sulfate aerosol, in particular R1 (Avallone et al., 1993; Dessler et al., 1993; Fahey et al., 1993; Toohey et al., 1993; Wilson et al., 1993; Keim et al., 1996). In their

study of the effects of moderate eruptions since Pinatubo, Zambri et al. (2019) found responses of as much as 20–50 pptv in simulated ensemble-mean monthly mean zonal-mean ClO from 70–5 hPa, but they showed an overall weaker correlation with SAD than that of HNO_3. In many cases, changes similar to those simulated were not seen in Aura MLS v4.2 bias-corrected ClO data. Those authors asserted that the precision of the MLS ClO measurements was too poor to permit detection of small anomalies, basing that statement on the MLS single-profile precision without considering the benefits of averaging.

3.3 HCl and $ClONO_2$

HCl and $ClONO_2$ are the main reservoirs of chlorine in the stratosphere. As discussed in Section 3.2, in the weeks following an explosive eruption, HCl can decrease through destruction by enhanced OH (since the rate of HCl loss through that mechanism is faster than its formation via $Cl+CH_4 \rightarrow HCl+CH_3$), and OH abundances may be especially elevated after the HT-HH water vapor injection. Heterogeneous chlorine chemistry (R2–R4) may also contribute if conditions allow. To our knowledge, however, HCl depletion induced by heterogeneous reactions on volcanic sulfate aerosol has never been observed.

MLS has captured direct volcanic injection of HCl into the stratosphere by a number of moderate eruptions (Prata et al., 2007; Theys et al., 2014; Carn et al., 2016), although peak volcanic HCl concentrations are likely underestimated since the vertical extent of the plumes is typically much smaller than the vertical resolution of MLS measurements. Only eight HCl profiles in mid-January 2022 exceeded the threshold used by Millán et al. (2022) to identify enhancements (7σ, corresponding to ∼5 ppbv of HCl through much of the domain), so no spikes can be expected to stand out in the HCl zonal means presented below. Scavenging by hydrometeors (liquid water drops or ice particles) or ash in eruption columns prevents much of the HCl emitted by major eruptions from reaching the stratosphere (Tabazadeh & Turco, 1993; Textor et al., 2003). Klobas et al. (2017) suggested that the very weak stratospheric HCl injection from Mt. Pinatubo (Mankin et al., 1992; Wallace & Livingston, 1992) is attributable to the extremely wet conditions caused by the coincidental passage of a tropical cyclone during the eruption, which may have allowed most of the degassed HCl to be scrubbed from its plume. Noting the contrast in HCl signals between the Sarychev and Kasatochi events despite their comparable magnitudes, Carn et al. (2016) postulated that the weaker HCl injection from the latter arose through more effective scavenging by abundant water in its plume since it erupted through a pre-existing crater lake. Similarly, the relatively modest HCl injection from HT-HH may have been a consequence of removal in the exceptionally moist and ice-rich environment in its plume (Carn et al., 2022). Nevertheless, it is conceivable that volcanogenic HCl could compensate to some degree any depletion caused by heterogeneous processing in the early post-eruption period.

If R2 or R3 are active to any significant extent, then $ClONO_2$ should decrease. On the other hand, some model simulations have shown mild increases in $ClONO_2$ (e.g., 20 pptv, ∼16%) under enhanced volcanic SAD conditions, since ClO (the limiting reactant in $ClO+NO_2+M \rightarrow ClONO_2+M$) increases (Kinnison et al., 1994; Berthet et al., 2017), while other modeling studies have found no discernible response in $ClONO_2$ (Zambri et al., 2019).

3.4 Ozone

The volcanically induced changes in stratospheric chlorine and nitrogen partitioning described above exacerbate chemical ozone destruction by the HO_x and ClO_x catalytic cycles (of primary importance in the lower stratosphere) but impede that by the NO_x cycle (the dominant ozone loss mechanism in the middle stratosphere). In addition to those direct chemical perturbations, increases in aerosol SAD affect radiative balance and hence the large-scale stratospheric circulation, with potentially considerable conse-

quences for the distribution of ozone (and other trace gases). Enhanced aerosol loading can also alter photolysis rates (e.g., Tie et al., 1994), further modifying ozone abundances. The net impact of these (in some cases competing) effects depends on the amount of sulfate aerosol produced from the emitted SO_2 and the latitude, altitude, and timing of the injection. Substantial reductions in lower-stratospheric and total column ozone have been observed and modeled after several previous volcanic eruptions (e.g., Dhomse et al., 2015; Hofmann & Solomon, 1989; Kilian et al., 2020; Millard et al., 2006; Naik et al., 2017; Randel et al., 1995; Solomon et al., 2016; Stone et al., 2017; Wilka et al., 2018, see also the citations listed at the beginning of this Section, and references therein). On the other hand, significant enhancement in ozone was observed in the southern midlatitudes above ∼26 km following Pinatubo; model simulations confirmed the important role of the NO_x loss cycle—and its suppression through R1 on volcanic sulfate aerosol—in determining the ozone budget at higher altitudes (Mickley et al., 1997).

4 Results

The unprecedented stratospheric impacts of HT-HH are clear in Figure 1, which provides an overview of the evolution of aerosol cross section from OMPS-LP (panel (a)) and water vapor from MLS (panel (b)) over their respective missions at 620 K potential temperature, a representative lower-stratospheric level that corresponds to ∼20–30 hPa or ∼24–26 km, depending on the EqL band and month. The previously reported initial low-latitude confinement, early northward extension, and eventual more efficient southward dispersion of the aerosol and water vapor plumes (Coy et al., 2022; Legras et al., 2022; Millán et al., 2022; Schoeberl et al., 2022; Taha et al., 2022) are evident. Large anomalies in other chemical constituents also arise in the aftermath of the eruption. A strong enhancement in HNO_3 quickly develops at the lowest latitudes and then gradually spreads poleward in both hemispheres over the next several months (Figure 1c). HNO_3 anomalies of comparable magnitude are not infrequent in the 18^+-year MLS record, however, and around mid-year the anomaly abruptly shifts sign, becoming strongly negative. In contrast, at this altitude the enhancement in ClO in the months after the eruption is unparalleled (Figure 1d), while HCl is largely unaffected initially but exhibits a severe low anomaly later in the year (Figure 1e). In the following subsections, we explore the extent to which these perturbations can be attributed to heterogeneous chemical processing. To elucidate the role of dynamics in controlling trace gas distributions, we also examine N_2O, a long-lived transport tracer whose vertical and meridional gradients in much of the lower stratosphere are opposite to those of HNO_3, HCl, and O_3 and which is therefore generally anticorrelated with those species in that region (Figure 1f). Finally, Figure 1g shows the unremarkable evolution of ozone in 2022.

We focus this analysis on the Southern Hemisphere (SH) midlatitudes, 38°S–54°S EqL, and the SH tropics, 6°S–22°S EqL. The former allows comparison of the volcano-induced perturbations in chlorine and nitrogen partitioning with those engendered by the Australian New Year's (ANY) fires in late 2019 / early 2020 (Santee et al., 2022; Solomon et al., 2022, 2023; Strahan et al., 2022) and is also characterized by somewhat better ACE-FTS data coverage; the latter experiences the largest HT-HH impacts on stratospheric composition but suffers from poor ACE-FTS sampling. We also briefly examine the intermediate region of the SH subtropics, 22°S–38°S EqL. Equivalent latitudes poleward of 54°S are ignored to minimize the confounding influence of seasonal chemical processing inside the Antarctic winter polar vortex.

In Figure 2 for the SH midlatitudes and similar figures for the other two EqL bands, we place the 2022 observations into climatological context and examine the evolution of chemical species in relation to sulfate aerosol loading, humidity, temperature, and transport. In the SH midlatitudes, we show 500 K (corresponding to ∼47–57 hPa or ∼20–21 km) to enable ANY comparisons and because the 2022 perturbations in ClO in that EqL band are largest there. In the SH subtropics and tropics, as in Figure 1, we again show 620 K,

where the ClO enhancements at those latitudes peak. The two preceding years, 2020 and 2021, are also highlighted. Figure 3 and similar figures provide information on the vertical extent of the perturbations. Anomalies are calculated as described in the relevant figure captions. Normalized anomalies are shown in the Supporting Information to facilitate comparison of changes across different quantities and EqL bands.

4.1 Southern Hemisphere Midlatitudes (38°S–54°S EqL)

We begin by looking at the SH midlatitudes, focusing on 500 K. Appreciable aerosol from HT-HH starts arriving in mid-April in this region, where it swiftly surpasses that resulting from ANY in 2020 and vastly exceeds the OMPS-LP mission envelope of behavior (Figure 2a). These results are not sensitive to the choice of aerosol data set examined (not shown; see Section 2). A corresponding positive anomaly in water vapor displays a slight lag in its arrival relative to aerosol in this EqL band; although water vapor mixing ratios at 500 K are above the climatological mean through most of 2020 and 2021 and remain so into 2022 (as noted also by Manney et al., 2023), they do not turn sharply upward at this level until mid-June (Figure 2b). Comparable delays in the upturn in water vapor relative to that in aerosol occur at most levels (cf. Figures 3h and 3i; see also Figure S2 in Supporting Information). Khaykin et al. (2022) similarly found slightly earlier appearance of aerosol than water vapor anomalies in the SH midlatitudes, again based on OMPS-LP and MLS data. The increases in midlatitude aerosol and water vapor seen at 500 K likely result from a combination of poleward flow along that isentrope and transport at higher levels (where the main volcanic cloud was initially deposited, as noted in the Introduction) followed by downward motion in this EqL band, either through gravitational settling in the case of aerosol or via diabatic descent for water vapor. We hypothesize that the discrepancy in the onset of the enhancements in aerosol and water vapor in the SH midlatitudes arises from a faster aerosol sedimentation rate as compared to the rate of water vapor descent in the stratospheric circulation.

Climatological temperatures in this EqL band at 500 K decrease from January into July; in 2022, temperatures are below average after mid-April and reach record lows in mid-August (Figure 2c). A sizeable negative anomaly in N_2O through much of 2021 continued into 2022, leading to low N_2O values at levels around 500 K for the first half of the year (Figure 2d; see also Figures 3f and 3m). Another transport tracer measured by MLS, CH_3Cl, exhibits similar, albeit weaker, departures from climatology in early 2022 (not shown), corroborating the picture seen in N_2O.

The evolution of the nitrogen species over the first few months of 2022 is more or less typical; although mixing ratios of N_2O_5 (Figure 2f), NO_x ($NO+NO_2$, Figure 2g), and HNO_3 (Figure 2h) at 500 K are initially below average, they all generally track the normal seasonal behavior at first. By early June, however, N_2O_5 values drop well below any previously observed in this region by ACE-FTS, and NO_x is also slightly below average. HNO_3 gradually increases relative to climatology until a very small positive anomaly develops in early June (Figures 2h). Slightly larger enhancements are visible at higher altitudes (540–620 K) from mid-April to mid-June (Figures 3c, 3j), but none stand out against the considerable dynamically driven year-to-year variability.

ClO at 500 K closely follows climatological mean evolution for the first few months, but it starts to climb steeply upward along with aerosol (but before water vapor) in early May (Figure 2l; the timing of the onset of the increases in ClO, aerosol, and water vapor can also be compared in Figure S2 in Supporting Information). Modest ClO enhancements of 10–20 pptv are seen on isentropic surfaces as low as 440 K and at least as high as 660 K, with peak positive anomalies approaching 40 pptv in early August at 500 K (Figures 3d, 3k). Non-negligible ClO anomalies (positive and negative) are also evident at higher altitudes, but MLS frequently records comparable vertically extensive features (Figure 3d); they likely arise through descent of changes in the mixing ratios at the secondary

peak in the ClO profile at around 1200 K in the upper stratosphere (not shown). Thus we focus on the ClO anomalies at 660 K and below. Given that those anomalies are significant at the $>2\sigma$ level for several months over a range of altitudes (Figure 3k), there is little doubt that they reflect real atmospheric features and not merely MLS measurement noise. Notable though they are, however, these enhancements are still substantially weaker than the maximum ClO perturbation of ∼80 pptv seen in the same EqL band in 2020 in the wake of the ANY fires (Figures 2l, 3d) and attributed to heterogeneous chlorine activation on smoke particles (Santee et al., 2022; Solomon et al., 2023; Strahan et al., 2022). Indeed, the 2022 ClO enhancements are not especially distinctive except near the peak in the anomaly profile at 500 K, where they lie at or above the range of variability observed over 2005–2019 from June to September and even exceed those in 2020 during August (Figure 2l). Consistent with the moderate increase in ClO, as discussed in Section 3.3, $ClONO_2$ shows small enhancements during the intervals of ACE-FTS sampling of this EqL band from June to August (Figure 2m).

Although HCl starts off quite a bit lower than normal, the suppressed values in early January 2022 reflect the continuation of a pre-existing negative anomaly that began in 2020 and persisted through 2021 (Figures 2n, 3e). The enduring below-average HCl abundances at the turn of the year may reflect a combination of transport effects and residual chlorine repartitioning after ANY (since aerosol, water vapor, and ClO also remained slightly perturbed through most of 2021; Figures 2a, 2b, 2l), but in any case they predate the eruption and could not have been caused by it. HCl increases fairly steadily for the first few weeks of 2022, reaching average values by mid-February. Thereafter, HCl generally follows the typical pattern of behavior until starting to drop sharply at most levels in mid-May (Figure 2n; also seen in Figures 3e, 3l). The downturn in HCl over May to August 2022 roughly parallels the much deeper ANY-induced depletion in HCl that occurred in earlier months in 2020 (Figure 2n). ACE-FTS indicates a very similar deficit in HCl starting in July and persisting through the end of 2022 (not shown). At face value, the significant concurrent but opposing changes in ClO and HCl point to the occurrence of substantial chemical processing. The story is not so simple, however.

At about the same time as the changes in the chlorine species, rather than increasing as would be expected from R1–R3 (see Section 3.1), HNO_3 rapidly decreases (Figure 2h), falling to very low values from July onward that at some levels redefine the bottom of the MLS mission envelope (not shown). This behavior is at odds with the changes in N_2O_5, whose values fall to near (or even below) zero, well outside the range previously observed during the ACE-FTS sampling intervals throughout the second half of the year (Figure 2f), and NO_x, which also sets new lower limits in October and November (Figure 2g). The lifetimes of N_2O_5 and NO_x are sufficiently short that their anomalies are almost completely driven by chemical perturbations, whereas HNO_3 is also subject to dynamical control. The abrupt shift in HNO_3, evident over a broad vertical range in the lower and middle stratosphere (Figure 3c), is mirrored by corresponding rapid increases in the transport tracer N_2O (Figures 2d, 3f). Scatter plots (Figure 4, left column) show reasonably tight anticorrelation between HNO_3 and N_2O through much of the lower stratosphere, including in 2022. At the levels where the mild positive HNO_3 anomaly is seen from mid-April to mid-June (540–620 K), two distinct clusters—one in the middle of the distribution from the early months of 2022, the other forming an extreme tail in the distribution later in the year—are linked by the points undergoing a steep decline in HNO_3 and growth in N_2O in July. But at no time during the year do the 2022 values stray dramatically from the historical HNO_3/N_2O relationship, indicating that the observed variations in HNO_3 in the SH midlatitudes are governed to a large extent by transport processes. The levels that show anomalously low values in the latter part of 2022 fall near or below below the peak in the HNO_3 profile, which is generally situated at around 600 K in the SH (e.g., Santee et al., 2004), while at potential temperatures above 700 K, HNO_3 anomalies are slightly positive at that time (Figures 3c, 3j). These signatures are con-

sistent with the markedly weaker diabatic descent and stronger poleward flow in the SH midlatitudes in the aftermath of HT-HH reported by Coy et al. (2022).

To help diagnose chemical effects, we approximate odd nitrogen, NO_y, as $2\times N_2O_5$ + NO_x + HNO_3 + $ClONO_2$, with HNO_3 taken from MLS and the others from ACE-FTS; together, these species account for about 97% of the stratospheric NO_y budget (e.g., Berthet et al., 2017). While the ACE-FTS (averages of sunrise and sunset occultations) and MLS measurements of these diurnally varying species are obtained at different local times, complicating precise quantification of NO_y, our purpose here is merely to qualitatively compare the behavior observed in 2022 with that in prior years. The ratios of N_2O_5 and NO_x to NO_y (Figures 2i, 2j) confirm that stratospheric nitrogen partitioning is shifted away from those species in the latter half of 2022. In contrast, HNO_3 makes up an anomalously large fraction of NO_y from June onward, redefining the previously observed range in early October and November (Figure 2k). These results suggest that heterogeneous HNO_3 production does take place in this EqL band in the months following HT-HH, but the signature of such processing in Figures 2h and 3c is overwhelmed by large countervailing transport effects.

The evolution of HNO_3 in the SH midlatitudes in 2022 differs from that observed by the predecessor MLS instrument on the Upper Atmosphere Research satellite (UARS), launched in September 1991, a few months after the June eruption of Mt. Pinatubo. UARS MLS HNO_3 retrievals in the equatorial region suffered from contamination by strongly volcanically enhanced SO_2 for the first ∼100 days of the mission, but retrievals at higher latitudes were unaffected by this artifact. UARS MLS first observed middle and high southern latitudes in November, by which time HNO_3 abundances were elevated throughout a broad swath of the hemisphere, with values at 585 K well outside the range measured by UARS MLS at similar times and locations during the rest of the mission (Santee et al., 2004). HNO_3 mixing ratios did not return to normal at the highest EqLs until the following June (1992), and the enhancement lingered for several months longer at midlatitudes, in line with residual volcanic aerosol there. Following Pinatubo, heating from absorption of longwave radiation by the volcanic aerosol altered the radiative balance and dynamics of the stratosphere, intensifying both the upwelling in the tropics and the downwelling in the SH extratropics (Aquila et al., 2012, 2013). This aerosol-induced perturbation in the mean circulation caused a positive anomaly in ozone in the SH midlatitudes (Aquila et al., 2013) and presumably had a similar effect on HNO_3, adding to any chemical enhancement that may have occurred. In contrast, as noted earlier, the radiative perturbation from the exceptional water vapor injection by HT-HH counteracted that from aerosol, resulting in net longwave cooling and weaker extratropical descent. The contrasting circulation changes likely account to a large extent for the apparently different HNO_3 responses to the two eruptions.

The strong influence of dynamics on HNO_3 in the second half of 2022 calls into question a primary chemical provenance for the steep mid-year dive in HCl. As with HNO_3, the rapid decrease in HCl coincides with an increase in N_2O (cf. Figures 2n and 2d). Scatter plots for HCl also show a bimodal structure in the lower stratosphere in 2022, with two discrete clumps linked by the points from July (Figure 4, middle column). In the case of HCl, however, notable deviations from the overall climatological HCl/N_2O relationship are seen at some levels. The conspicuous departure from anticorrelation in the grey dots at 460–620 K is a signature of heterogeneous chlorine activation on smoke particles from ANY (Santee et al., 2022). While behavior as clearly anomalous as that in 2020 is not evident in 2022, points from July / August onward at 460–660 K (the domain over which ClO displays enhancements) do fall in positions that were previously unoccupied in the distribution to a much greater extent than they did for HNO_3. To help disentangle dynamical and chemical effects, we define inorganic chlorine, Cl_y, as ClO + $ClONO_2$ + HCl, with ClO and HCl from MLS and $ClONO_2$ from ACE-FTS. Stratospheric transport is known to play a key role in controlling the Cl_y distribution (Strahan et al., 2014).

The ratios of ClO and $ClONO_2$ to Cl_y (Figures 2o, 2p) confirm that stratospheric chlorine partitioning is shifted toward those species, especially ClO, in the second half of 2022. The HCl/Cl_y ratios, on the other hand, reveal an anomalously small contribution to inorganic chlorine from HCl in early June, July, and August (Figure 2q). We surmise that, although the pronounced reduction in SH midlatitude HCl in the latter part of 2022 is chiefly governed by transport, HCl abundances are also being suppressed by chemical processing.

To obtain a qualitative sense of the onset of anomalous post-HT-HH partitioning via reactions R1–R5 at 500 K, where the observed perturbations in the chlorine species in this EqL band are largest, Figure 5 compares their respective first-order rate constants in 2022 to those in 2021. The rate constant for a heterogeneous reaction is proportional to its reaction probability (γ value, Figure S1 in Supporting Information), SAD, and the thermal velocity of the molecule. The calculations in Figure 5 are based on the water vapor and temperature values shown in Figure 2, but they use constant abundances for the other gas-phase species as well as a fixed SAD of $2\,\mu m^2\,cm^{-3}$, representing background conditions. Thus, these results are intended to illuminate only the influence of water vapor and temperature on R1–R5; they take no account of the enhanced aerosol loading, the true chlorine species mixing ratios, or the evolution of those quantities over the year. While using an enhanced SAD value for 2022 would more accurately characterize post-HT-HH conditions, doing so would affect the rate constants for R1–R5 proportionally and thus would reveal no additional information about the relative effectiveness of those reactions beyond that provided in Figure 5. Calculation of actual reaction rates, and hence full quantification of the individual contributions of R1–R5 to the observed repartitioning, requires detailed chemical modeling beyond the scope of this analysis. Nevertheless, Figure 5 provides useful insight. The rate constants for R2–R4 are slightly higher in 2022 than in the preceding year from late July onward, not dissimilar to the timing of the perturbations in ClO and HCl (i.e., the HCl/Cl_y ratio). This might suggest a role for those reactions. However, their rate constants are still several orders of magnitude smaller than those for R1 and R5. Taking the reciprocal of the maximum 2022 rate constants (which are in units of s^{-1}) in Figure 5 yields approximate chemical lifetimes for the gas-phase reactants of 1 day for R1, 10 months for R2, 60 years for R3, 40 years for R4, and 5 hours for R5. Our results are in line with the modeling work by Robrecht et al. (2019), who demonstrated that R2 and R3 (and by implication also R4) do not become effective until temperatures fall below 205 K even for very high water vapor mixing ratios of 20 ppmv and volcanic conditions of 10× background SAD. Although at its peak the EqL-mean aerosol cross section in this region is enhanced by about a factor of 20, the maximum water vapor values are just over 5 ppmv, and minimum temperatures are ∼210 K. We conclude that, despite the heavy aerosol loading, excess moisture, and strong cooling in the 2022 SH midlatitudes following HT-HH, ambient conditions remain unfavorable for R2–R4, and only R1 and R5 are at play in producing the observed moderate chlorine activation. This is in contrast to the situation following ANY in 2020, when the high solubility of HCl in aged stratospheric smoke particles apparently triggered heterogeneous chlorine activation, in particular via R3, under relatively warm conditions in the SH midlatitudes (Solomon et al., 2023).

Finally, an obvious question is whether the mild enhancement in reactive chlorine in 2022 had a discernible impact on ozone concentrations. As noted by Santee et al. (2022), although the strong and sustained midlatitude chlorine activation that occurred in the wake of ANY was unprecedented in the satellite record, it was still an order of magnitude or more weaker than that in a typical winter polar vortex. They found no conclusive observational evidence of significant ANY-induced chemical ozone destruction; rather, they attributed the anomalously low ozone observed in the SH midlatitudes in 2020 (and until midway through 2021) largely to transport effects, as did Strahan et al. (2022). In contrast, other studies argued that heterogeneous chemistry on ANY smoke particles did give rise to detectable ozone loss (e.g., Rieger et al., 2021; Solomon et al., 2022, 2023;

Yu et al., 2021). Given that the degree of chlorine activation in 2022 is about half that following ANY and the large-scale dynamical perturbations are far greater, we expect the evidence of chemical ozone destruction from HT-HH to be even more equivocal.

Figure 2e shows that the behavior of ozone in the SH midlatitude lower stratosphere in 2022 is not dissimilar to that in 2020, with ozone mixing ratios generally low but not outside the range of previously observed variability. Below 600 K, the changes in ozone track those in HNO_3 and HCl; above that level, ozone becomes positively correlated with N_2O in this EqL band and increases in the second half of the year (Figures 1g, 3g, 3n). Although the 2022 O_3/N_2O correlations show two distinct populations in the early and late months of the year at lower potential temperatures, as they do also for HNO_3 and HCl, for the most part the points do not lie outside the typical transport-controlled distribution (Figure 4, right column). Thus MLS measurements indicate that the minor increases in ClO provoked by HT-HH do not result in appreciable chemical ozone loss in the SH midlatitude lower stratosphere in 2022.

4.2 Southern Hemisphere Subtropics (22°S–38°S EqL)

The evolution in the SH subtropics at 620 K is similar to that at midlatitudes and is summarized only briefly. Aerosol increases rapidly almost immediately after the eruption, reaching maximum values between April (620–660 K) and August (460–500 K) that are larger at a given level than those at more poleward EqLs (Figure 6a; Figures S3a, S3h in Supporting Information). HNO_3 ticks upward in late January above 560 K (Figure 6h; Figures S3c, S3j in Supporting Information). This positive anomaly, though still small, starts earlier, achieves a larger magnitude (>0.6 ppbv at 580–660 K in April), and extends to higher altitudes than seen in the 38°S–54°S EqL band. Maximum values protrude above the mission envelope (Figure 6h), albeit only marginally and for a short interval in some cases. HNO_3 values continue to slowly rise in subsequent months at the highest altitudes (Figure S3j in Supporting Information). At lower levels, however, they decline, with a particularly precipitous drop in May–June over 540–700 K, and then remain anomalously low through the end of the year. The downturn starts sooner but is less abrupt than that seen at midlatitudes, and for the most part HNO_3 values do not dip below the MLS mission envelope. Although the sparser sampling of ACE-FTS in this EqL band compromises identification of anomalies, slightly depressed N_2O_5 (Figures 6f, 6i) and NO_x (Figures 6g, 6j) in later months again suggest repartitioning within the odd nitrogen family, and elevated HNO_3/NO_y ratios (Figure 6k) are consistent with some chemical production of HNO_3.

HCl follows the climatological mean for the first few months of 2022 before falling fairly steeply to values lower than any previously observed above 550 K (Figure 6n); below that level, the record HCl deficits in 2020 arising from ANY still stand. The decrease in HCl begins about a month earlier than in the 38°S–54°S EqL band. As before, scatter plots (Figure S4 in Supporting Information, left and middle columns) show two separated clusters in 2022 in much of the lower stratosphere, connected by points with rapidly decreasing HNO_3 and HCl but increasing N_2O, in this case during May–June. However, above 460 K the 2022 HCl values lie in previously unpopulated areas of the distribution to a much greater extent than at midlatitudes. In addition, the HCl/Cl_y ratios are indicative of chlorine repartitioning from April onward (Figure 6q). ClO shows an even more prominent signature of chemical processing, with significant positive anomalies appearing over 460–700 K as early as March and reaching maxima of as much as 30–35 pptv in May–July, depending on the level, as the peak in the ClO anomaly profile gradually descends in concert with the downward progression of the sulfate aerosol (Figures S3d, S3k in Supporting Information). At most levels, the 2022 ClO abundances sit near or above the top of the mission envelope for a few months (e.g., Figure 6l); at and above 620 K, they exceed the ANY enhancements at all times, while at lower levels they are initially smaller than 2020 values but then stay elevated through the end of the year (Fig-

ure S3d in Supporting Information). The timing of the buildup, peak values, and decay of the ClO anomaly coincides closely with that of the aerosol anomaly but generally precedes that of the water vapor anomaly (Figure S2 in Supporting Information). Although the general picture is similar to that in the SH midlatitudes, the relationship between active chlorine and aerosol cross section is clearer in this EqL band.

As with HNO_3 and HCl, ozone mixing ratios briefly dip below the climatological mean at 620 K in June–July, mirroring the bump up in N_2O; thereafter, ozone rises steadily until it skirts the top of the observed range from October onward (Figure 6e). None of the analyses, including the scatter plots in Figure S4 in Supporting Information (right column), show patterns indicative of significant chemical ozone loss in 2022.

4.3 Southern Hemisphere Tropics (6°S–22°S EqL)

In the SH tropics, aerosol (Figures 7a, 8a, 8h) and water vapor (Figures 7b, 8b, 8i) are abruptly enhanced through much of the lower stratosphere immediately after the eruption. At the levels of interest here, the choice of aerosol dataset used makes no material difference to these results. A warming trend throughout the stratosphere in this EqL band prior to the event is reversed, with temperatures dropping by ∼2 K during February (Figure 7c; see also Schoeberl et al., 2022).

Concomitant with these changes, HNO_3 increases rapidly above 500 K (Figures 8c, 8j), overshooting the previously observed range by early February, with values then near or above the top of the envelope through the first half of the year (Figure 7h). Large anomalies of ∼0.7–0.8 ppbv are seen from 580–800 K (Figures 8j). The HNO_3/N_2O scatter plots (Figure 9, left column) show that the March–July points lie at the outer edge of or slightly apart from the main distribution at most levels, suggesting that transport is not the sole factor controlling HNO_3 abundances at this time; rather, the observed behavior is indicative of heterogeneous processing. This determination is substantiated by the very low N_2O_5 (Figures 7f, 7i) and NO_x (Figures 7g, 7j) values, as well as the greatly elevated HNO_3/NO_y ratios (Figure 7k) throughout 2022. Although the picture is unfortunately fragmentary because of the poor ACE-FTS sampling at low latitudes, the 2022 values of all of these quantities are clearly highly anomalous.

After rising steadily for a few weeks, however, HNO_3 mixing ratios then level off and remain approximately flat until June, when they start to increase again, largely following the typical seasonal pattern (Figure 7h). We interpret the March–May plateau in HNO_3 as evidence of the saturation of N_2O_5 hydrolysis. The amount of N_2O_5 available to participate in R1 is limited by its formation (mainly from the recombination of NO_2 and NO_3 at night, whose rate depends quadratically on NO_x). When aerosol SAD exceeds a certain threshold, N_2O_5 is hydrolyzed as fast as it can be formed, and further increases in SAD do not affect the rate of conversion of NO_x to HNO_3 by R1 (e.g., Fahey et al., 1993; Tie et al., 1994). Although ACE-FTS coverage in the tropics is too sparse to permit diagnosis of saturation in the NO_x data, this mechanism may explain why HNO_3 production appears to stall by early March at many levels (Figure 8j), while aerosol (Figure 8h) and water vapor (Figure 8i) are still increasing. It may also account for the continuous gradual increase in HNO_3 in April at higher potential temperatures (660–850 K), as well as the lack of strong enhancement at lower potential temperatures (460, 500 K) despite the presence of substantial aerosol there, since saturation occurs for relatively lower aerosol amounts at lower altitudes (e.g., Mills et al., 1993). Similarly, Santee et al. (2004) reported considerably greater impact from Pinatubo on HNO_3 abundances at higher (585 K) than at lower (420, 465 K) potential temperatures based on UARS MLS measurements and attributed the differences to R1 saturation.

The evolution of ClO is also consistent with substantial sustained heterogeneous processing in this EqL band in 2022. Significant enhancements appear by mid-January from 500 to 700 K, with maxima as large as 40–45 pptv at 580–660 K in March (Figure 8k),

far exceeding the previously observed range of behavior (Figures 7l, 8d; see also Figure 1d). The enhancement slowly decays after April, but mixing ratios remain elevated over much of the domain through the end of the year. A secondary MLS ClO product retrieved from radiances in a different spectral band than that used in generating the standard ClO data indicates a similar (albeit noisier) persistent strong enhancement (not shown). $ClONO_2$ is also high during the brief windows of ACE-FTS sampling through most of the year (Figures 7m, 7p). As with HNO_3, after an initial steep rise, ClO values then remain more or less steady for the next several months (Figures 7l, 8k). A similar nonlinear response to increasing aerosol SAD seen in airborne in situ ClO measurements after the eruption of Mt. Pinatubo was attributed to the saturation of N_2O_5 hydrolysis on sulfate aerosols (Avallone et al., 1993; Fahey et al., 1993). The aircraft campaigns also found the largest ClO enhancements at the lowest latitudes sampled (Avallone et al., 1993). Thus, our results are qualitatively in accord with the earlier in situ findings. In addition, the MLS-based ClO enhancements are comparable to post-eruption values simulated in several modeling studies (e.g., Kinnison et al., 1994; Tie et al., 1994; Zambri et al., 2019). On the other hand, Zambri et al. (2019) also examined MLS ClO measurements after multiple moderate-magnitude eruptions in the post-Pinatubo era (see Section 3.2) and found no enhancements matching those modeled, possibly because the HT-HH impact on stratospheric chlorine activation in the SH tropics greatly surpasses that of any prior event.

In the immediate aftermath of the HT-HH eruption, as HNO_3 and ClO shoot up, HCl displays a modest (<0.08 ppbv) but fairly sharp decrease over a limited altitude range (540–660 K; Figure 8l). This dip in January, which is not seen at higher latitudes, places the 2022 HCl values at or near the bottom of the envelope at those altitudes in February and March (Figure 7n). Given that N_2O is generally low at this level at this time in 2022 (Figures 7d, 8f), correspondingly high HCl mixing ratios would have been expected. After its initial decrease, HCl follows climatological patterns (i.e., deviations from the mean remain essentially flat) for a few months, echoing the plateau in ClO (Figures 7n, 8l) until dynamically driven changes—negative anomalies below 660 K, positive anomalies above (Figures 8e, 8l)—develop in the latter part of 2022. Although the HCl/N_2O correlations are not especially unusual for the first half of the year, from about July onward they stand apart from the typical relationships at and above 620 K (Figure 9, middle column). This behavior likely signifies continuing mid-year chemical suppression of HCl, in consonance with the evolution of ClO. The extremely low HCl/Cl_y ratios seen during the intervals of ACE-FTS coverage (Figure 7q) confirm the depletion of HCl through heterogeneous chemical processing.

In the 620–660 K layer, close to the altitude of the maximum HT-HH water vapor injection (Figure 8i; Millán et al., 2022), the steep increases in HNO_3 and ClO and the decrease in HCl in the first weeks after the eruption occur nearly simultaneously with the pulses in both water vapor and aerosol (Figure S2 in Supporting Information). Below that layer, however, HNO_3, ClO, and HCl change more or less in unison with the increase in water vapor, while the aerosol curves slope upward more gently and peak weeks to months later. This behavior in the SH tropics differs from that in the subtropics and midlatitudes, where, as discussed in the previous section, ClO enhancement generally tracks the evolution of aerosol more closely than that of water vapor at altitudes below 600 K. Climate model simulations have shown that the extraordinary magnitude of the HT-HH water vapor anomaly halved the SO_2 lifetime, leading to more rapid coagulation of larger sulfate particles than is typical (Zhu et al., 2022). The slower buildup in aerosol at lower potential temperatures in the tropics may reflect the longer time required for sulfate formation at less water-rich levels and/or the timescale for sedimenting particles from above to reach those levels. The observed latitudinal differences in the relationships between aerosol, water vapor, and reactive chlorine may arise because, by the time a substantial portion of the HT-HH plume disperses to the SH subtropics, the conversion to sulfate aerosol is well underway. Nevertheless, sufficient sulfate aerosol to enable heterogeneous processing is clearly present soon after the eruption even at lower al-

titudes in the tropics, as evidenced by the rapid rise in HNO_3 and ClO there (Figures 8j, 8k; Figure S2 in Supporting Information).

In contrast to R1, reactions R2 and R5 are not subject to saturation in the lower stratosphere. Thus, the fact that HNO_3 and ClO do not continue to increase in tandem with aerosol implies that R1 is playing a dominant role in their production. Moreover, a larger decrease in HCl, as well as a decrease (rather than an increase) in $ClONO_2$, would be expected if direct heterogeneous chlorine activation were proceeding. The results of our rate constant calculations (Figure 10) support this supposition. Although the ambient (temperature, water vapor) conditions in 2022 increase the rate constants for R2–R4 considerably over their respective 2021 values starting in late January / early February, they remain several orders of magnitude smaller than those for R1 and R5. Therefore, we conclude that, as exceptional as the aerosol and water vapor enhancements in this EqL band are, they are not sufficient to promote R2–R4 to any significant extent under the colder than normal but still relatively (compared to polar winter) warm conditions that prevail in the first half of 2022 (Figure 7c).

Figures 5 and 10 show that the rate constant for R5 is as much as 5–6 times faster than that for R1. Photolysis of the HOBr and HNO_3 resulting from $BrONO_2$ hydrolysis is an important source of OH, rivalling that from nitrogen chemistry under conditions of volcanically enhanced aerosol; indeed, about half of the simulated changes in stratospheric chlorine species after the Sarychev eruption were attributed to elevated OH abundances from R5 (Berthet et al., 2017). In addition to $ClONO_2$ and $BrONO_2$ hydrolysis as a source of OH, the excess water vapor from HT-HH likely amplifies direct OH formation from H_2O oxidation; model simulations by Zhu et al. (2022) show increases in OH in the SH tropics immediately following the eruption compared to a run with no water vapor injection. Unfortunately, MLS no longer measures OH itself, but measurements of HO_2 (the other main member of the HO_x family) are available from MLS in the middle stratosphere; those data indicate some enhancement in early 2022 (Figure S5 in Supporting Information). As noted above, the small decreasing tendency in HCl levels off at approximately the same time as the increases in HNO_3 and ClO; this behavior may point to saturation and hence the influence of enhanced OH arising from R1, rather than from R5 or from the additional water vapor from HT-HH. Again, full quantification of the effectiveness of the different processes contributing to OH production (and hence chlorine repartitioning) requires detailed chemical modeling beyond the scope of this study.

Finally, although heterogeneously driven chemical loss typically plays little or no role in determining ozone abundances in the tropics, we investigate whether the unprecedented degree of chlorine activation in the 500–700 K layer following HT-HH leads to perceptible reductions in ozone. At 620 K, ozone displays substantial variability throughout 2022, rising and falling fairly rapidly at various times and occasionally redefining the top of the mission envelope (Figure 7e). Of particular note is the steep decline in March and early April, which coincides with the maximum enhancement in ClO (Figure 7l) and thus could be a sign of chemical loss. However, ozone mixing ratios at this level barely fall below the climatological mean before beginning to increase again at the end of May, and surrounding levels also see only small decreases (Figure 8n). Ozone remains largely anticorrelated with N_2O in the tropics at this altitude (cf. Figures 8f and 8g), and the O_3/N_2O scatter plots show no hint of abnormally low O_3 values suggestive of depletion at any point during the year (Figure 9, right column). Therefore, any signature of chlorine-catalyzed ozone loss that may be taking place in the lower stratosphere is masked by much larger changes due to transport. On the other hand, points from the latter half of 2022 fall well outside the previously observed O_3/N_2O distribution at 660 K (and higher levels; not shown). These anomalously high ozone values may reflect diminished efficiency of the NO_x catalytic loss cycle, which dominates ozone destruction in the middle stratosphere (see Section 3.4).

5 Summary and Conclusions

The eruption of HT-HH in January 2022 caused a substantial perturbation in stratospheric aerosol loading, which, although not unprecedented in the modern instrumental era, was nevertheless the largest in the last several decades. Even more noteworthy was the uniquely extreme enhancement in stratospheric water vapor. The submarine vent erupted at a "Goldilocks" depth—sufficiently shallow that the pressure of the overlying water did not dampen the power of the blast, sufficiently deep to allow extensive magma-seawater interaction (Witze, 2022). In addition, the plume was injected at an advantageous location, as lofting into lower altitudes or higher latitudes where air is colder would have resulted in smaller water vapor anomalies (Schoeberl et al., 2022). The excess moisture led to strong stratospheric cooling that in turn induced anomalous circulation patterns.

In this study, we use constituent profile measurements from Aura MLS and ACE-FTS, aerosol extinction from OMPS-LP, and meteorological parameters from MERRA-2 to investigate the extent to which the dense aerosol, high humidity, and strong cooling brought about by HT-HH prompted heterogeneous chemical reactions to occur in regions where they are not normally active to a significant degree. We look for signatures of chlorine and nitrogen repartitioning in the SH midlatitudes, subtropics, and tropics over a range of altitudes in the lower and middle stratosphere. Calculated rate constants for the heterogeneous reactions R1–R5 provide insights into their relative importance in altering trace gas distributions. Ozone is also examined for evidence of chemical loss as a result of the eruption.

In the SH midlatitudes (38°S–54°S EqL), N_2O_5 and NO_x exhibit considerable decreases at 500 K in the second half of 2022 that are consistent with heterogeneous processing on HT-HH aerosol. Although enhancements in HNO_3 would be expected in association with the reductions in N_2O_5 and NO_x, strong dynamical effects instead lead to unusually low HNO_3 values that in some cases redefine the previously observed range, and HNO_3 production only becomes apparent in the HNO_3/NO_y ratios. Signs of heterogeneous chlorine activation are more compelling, with a positive anomaly in ClO reaching 35–40 pptv at its peak near 500 K from June through August, accompanied by an increase in $ClONO_2$. Although significant at the $>2\sigma$ level, however, the ClO anomaly is only marginally outside the envelope of previous behavior over a narrow layer for a few months. Transport effects dominate the evolution of HCl in the latter part of 2022, but chemically induced deficits in HCl that mirror the enhancements in ClO and $ClONO_2$ are evident in the HCl/Cl_y ratios. Perturbations in all chlorine species are considerably weaker than those measured at these levels in this EqL band in 2020 in the aftermath of the ANY fires. Rate constant calculations suggest that, despite the unusually moist and cool conditions in the SH midlatitude stratosphere following HT-HH, heterogeneous chlorine activation reactions R2–R4 are not at work to any significant extent, and R1 and R5 (hydrolysis of N_2O_5 and $BrONO_2$, respectively) are primarily responsible for the observed composition changes. Evidence of widespread and persistent HT-HH-induced chlorine and nitrogen repartitioning is even clearer in the SH subtropics (22°S–38°S EqL), but the signatures of heterogeneous processing in HNO_3 and HCl are again obscured by dynamical influences.

In the SH tropics (6°S–22°S EqL), unambiguous signatures of substantial heterogeneous processing appear over a broad vertical domain almost immediately after the eruption. Substantial repartitioning of both the nitrogen and the chlorine families occurs, as evidenced by depletion of N_2O_5 and NO_x together with enhancement of HNO_3, ClO, and $ClONO_2$. Unlike at higher latitudes, in this EqL band HCl also decreases rapidly right after the eruption, and, in the second half of 2022, it displays extremely low HCl/Cl_y ratios, as well as notable departures from the typical HCl/N_2O correlations. These patterns all point to significant chemical suppression of HCl. To our knowledge, volcanically induced HCl depletion has not been reported previously. After initially rising steeply,

HNO_3 and ClO essentially plateau, maintaining fairly constant anomalies (of as much as 0.7–0.8 ppbv and 40–45 pptv, respectively) for several months. This behavior is consistent with the saturation of N_2O_5 hydrolysis, suggesting that R1 is the primary mechanism for the production of HNO_3 and, after associated gas-phase chemistry, the increases in ClO and $ClONO_2$. Enhancements in OH brought about by the excess water vapor from HT-HH may also play a role in the chlorine repartitioning. As at midlatitudes, rate constant calculations imply that reactions R2–R4 play no significant role in the observed composition changes. Quantification of the relative contributions of the different processes perturbing stratospheric composition in the wake of HT-HH will require detailed modeling efforts.

The moderate enhancements in reactive chlorine seen throughout the SH mid- and low-latitude lower stratosphere following HT-HH do not lead to appreciable chemical loss of ozone; rather, lower-stratospheric ozone in those regions remains primarily controlled by transport processes. The lack of chemical ozone depletion in 2022 substantial enough over an area extensive enough to be perceptible in the EqL means examined here is not surprising. Although the 2022 ClO anomalies are unprecedented in the tropics and subtropics and are exceeded only by those induced by ANY in the midlatitudes, they are still only about half as large as those arising from that event. Moreover, the ClO perturbations caused by ANY were themselves more than an order of magnitude weaker than the enhancements in typical winter polar vortices. In the middle stratosphere, by contrast, reduced NO_x may have decreased the efficiency of that loss cycle, leading to mild increases in ozone at and above 660 K.

The strong positive stratospheric aerosol anomaly from HT-HH has already substantially abated, and, assuming no further major perturbations, stratospheric aerosol loading is expected to return to pre-eruption levels by around mid-2023 (Khaykin et al., 2022). In contrast, stratospheric water vapor abundances remain historically high, with the extreme enhancement likely to endure for several more years (Khaykin et al., 2022; Millán et al., 2022). The HT-HH water vapor plume was effectively excluded from the 2022 Antarctic polar vortex and thus had little or no impact on that year's ozone hole; similarly, it did not reach northern high latitudes in time to influence Arctic ozone loss in boreal spring 2023 (Manney et al., 2023). However, the sustained HT-HH water vapor enhancement is expected to significantly affect Antarctic and Arctic vortex chemistry and ozone loss during their upcoming 2023 and 2023/2024 winter/spring seasons. Our ability to assess the impact of HT-HH on stratospheric chemistry and polar ozone depletion over the next few years will depend strongly on the continuing availability of satellite observations from Aura MLS and ACE-FTS.

6 Data Availability Statement

The data sets used here are publicly available, as follows:

- Aura MLS Level 2 data (Lambert, Read, & Livesey, 2020; Manney et al., 2020; Santee et al., 2020; Froidevaux et al., 2020; Lambert, Livesey, & Read, 2020; Schwartz et al., 2020; Wang et al., 2020): `https://disc.gsfc.nasa.gov/datasets?page=1&keywords=AURA%20MLS`
- Aura MLS Derived Meteorological Products (DMPs; Manney & Millán, 2007–present): `https://mls.jpl.nasa.gov/eos-aura-mls/dmp` (registration required)
- ACE-FTS 4.1/4.2 data: `http://www.ace.uwaterloo.ca` (registration required at `https://databace.scisat.ca/l2signup.php`)
- ACE-FTS v4.1/4.2 error flags (Sheese & Walker, 2020): `https://doi.org/10.5683/SP2/BC4ATC`
- OMPS-LP L2 Aerosol Extinction Vertical Profile swath multi-wavelength daily 3slit Collection 2 V2.0 data (Taha, 2020): `https://doi.org/10.5067/CX2B9NW6FI27`

- MERRA-2 (Global Modeling and Assimilation Office (GMAO), 2015): `https://disc.sci.gsfc.nasa.gov/uui/datasets?keywords=%22MERRA-2%22`

Acknowledgments

We thank the MLS team at JPL, especially P. Wagner and B. Knosp, for retrieval processing and computational and data management support; the ACE-FTS team for producing and making available their data, especially P. Sheese and K. Walker for providing ACE-FTS v4 quality information and screening criteria; the OMPS-LP team for producing and making available their data; and NASA's GMAO for producing and making available their assimilated data products. G.L. Manney was supported by the JPL Microwave Limb Sounder team under a JPL subcontract to NWRA. Work at the Jet Propulsion Laboratory, California Institute of Technology, was carried out under a contract with the National Aeronautics and Space Administration (80NM0018D0004).

References

Adams, C., Bourassa, A. E., McLinden, C. A., Sioris, C. E., von Clarmann, T., Funke, B., ... Degenstein, D. A. (2017). Effect of volcanic aerosol on stratospheric NO_2 and N_2O_5 from 2002–2014 as measured by Odin-OSIRIS and Envisat-MIPAS. *Atmos. Chem. Phys.*, *17*, 8063–8080. doi: 10.5194/acp-17-8063-2017

Anderson, J. G., Wilmouth, D. M., Smith, J. B., & Sayres, D. S. (2012). UV dosage levels in summer: Increased risk of ozone loss from convectively injected water vapor. *Science*, *337*, 835–839. doi: 10.1126/science.1222978

Aquila, V., Oman, L. D., Stolarski, R. S., Colarco, P. R., & Newman, P. A. (2012). Dispersion of the volcanic sulfate cloud from a Mount Pinatubo-like eruption. *J. Geophys. Res.*, *117*. doi: 10.1029/2011JD016968

Aquila, V., Oman, L. D., Stolarski, R. S., Douglass, A. R., & Newman, P. A. (2013). The response of ozone and nitrogen dioxide to the eruption of Mt. Pinatubo at southern and northern midlatitudes. *J. Atmos. Sci.*, *70*, 894–900. doi: 10.1175/JAS-D-12-0143.1

Arnold, F., Bührke, T., & Qiu, S. (1990). Evidence for stratospheric ozone-depleting heterogeneous chemistry on volcanic aerosols from El Chichón. *Nature*, *348*, 49–50.

Avallone, L. M., Toohey, D. W., Proffitt, M. H., Margitan, J. J., Chan, K. R., & Anderson, J. G. (1993). In situ measurements of ClO at mid-latitudes: Is there an effect from Mt. Pinatubo? *Geophys. Res. Lett.*, *20*, 2519–2522. doi: 10.1029/93GL02418

Bekki, S., & Pyle, J. A. (1994). A two-dimensional modeling study of the volcanic eruption of Mount Pinatubo. *J. Geophys. Res.*, *99*, 18,861–18,869.

Berthet, G., et al. (2017). Impact of a moderate volcanic eruption on chemistry in the lower stratosphere: balloon-borne observations and model calculations. *Atmos. Chem. Phys.*, *17*, 2229–2253. doi: 10.5194/acp-17-2229-2017

Boone, C. D., Bernath, P. F., Cok, D., Jones, S. C., & Steffen, J. (2020). Version 4 retrievals for the atmospheric chemistry experiment Fourier transform spectrometer (ACE-FTS) and imagers. *J. Quant. Spectrosc. Radiat. Transfer*, *247*. doi: 10.1016/j.jqsrt.2020.106939

Bourassa, A. E., Zawada, D. J., Rieger, L. A., Warnock, T. W., Toohey, M., & Degenstein, D. A. (2023). Tomographic retrievals of Hunga Tonga-Hunga Ha'apai volcanic aerosol. *Geophys. Res. Lett.*, *50*. doi: 10.1029/2022GL101978

Butchart, N., & Remsberg, E. E. (1986). The area of the stratospheric polar vortex as a diagnostic for tracer transport on an isentropic surface. *J. Atmos. Sci.*, *43*, 1319–1339. doi: 10.1175/1520-0469(1986)043⟨1319:TAOTSP⟩2.0.CO;2

Carn, S. A., Clarisse, L., & Prata, A. J. (2016). Multi-decadal satellite measurements of global volcanic degassing. *J. Volcanol. Geotherm. Res.*, *311*, 99–134. doi: 10.1016/j.jvolgeores.2016.01.002

Carn, S. A., Krotkov, N. A., Fisher, B. L., & Li, C. (2022). Out of the blue: Volcanic SO_2 emissions during the 2021–2022 eruptions of Hunga Tonga-Hunga Ha'apai (Tonga). *Front. Earth Sci.*, *10*. doi: 10.3389/feart.2022.976962

Carr, J. L., Horváth, Á., Wu, D. L., & Friberg, M. D. (2022). Stereo plume height and motion retrievals for the record-setting Hunga Tonga-Hunga Ha'apai eruption of 15 January 2022. *Geophys. Res. Lett.*, *49*. doi: 10.1029/2022GL098131

Coffey, M. T. (1996). Observations of the impact of volcanic activity on stratospheric chemistry. *J. Geophys. Res.*, *101*, 6767–6780.

Coy, L., Newman, P. A., Wargan, K., Partyka, G., Strahan, S. E., & Pawson, S. (2022). Stratospheric circulation changes associated with the Hunga Tonga-Hunga Ha'apai eruption. *Geophys. Res. Lett.*, *49*. doi: 10.1029/2022GL100982

David, S. J., Murcray, F. J., Goldman, A., Rinsland, C. P., & Murcray, D. G. (1994). The effect of the Mt. Pinatubo aerosol on the HNO_3 column over Mauna Loa, Hawaii. *Geophys. Res. Lett.*, *21*, 1003–1006.

Dessler, A. E., et al. (1993). Balloon-borne measurements of ClO, NO, and O_3 in a volcanic cloud: An analysis of heterogeneous chemistry between 20 and 30 km. *Geophys. Res. Lett.*, *20*, 2527–2530. doi: 10.1029/93GL02419

Dhomse, S. S., Chipperfield, M. P., Feng, W., Hossaini, R., Mann, G. W., & Santee, M. L. (2015). Revisiting the hemispheric asymmetry inmidlatitude ozone changes following the Mount Pinatubo eruption: A 3-d model study. *Geophys. Res. Lett.*, *42*. doi: 10.1002/2015GL063052

Fahey, D. W., Kawa, S. R., Woodbridge, E. L., Tin, P., Wilson, J. C., Jonsson, H. H., ... Chan, K. R. (1993). In situ measurements constraining the role of sulphate aerosols in mid-latitude ozone depletions. *Nature*, *363*, 509–514. doi: 10.1038/363509a0

Froidevaux, L., Livesey, N., & Read, W. (2020). *MLS/Aura Level 2 hydrogen chloride (HCl) mixing ratio V005, Greenbelt, MD, USA, Goddard Earth Sciences Data and Information Services Center (GES DISC)* [dataset]. doi: https://doi.org/10.5067/Aura/MLS/DATA2509

Gelaro, R., et al. (2017). The Modern-Era Retrospective Analysis for Research and Applications, Version 2 (MERRA-2). *J. Climate*, *30*, 5419–5454. doi: 10.1175/JCLI-D-16-0758.1

Global Modeling and Assimilation Office (GMAO). (2015). *MERRA-2 inst3_3d_asm_nv: 3d, 3-hourly,instantaneous, model-level, assimilation, assimilated meteorological fields v5.12.4, Greenbelt, MD, USA, Goddard Earth Sciences Data and Information Services Center (GES DISC)* [dataset]. doi: 10.5067/WWQSXQ8IVFW8

Gupta, A. K., Bennartz, R., Fauria, K. E., & Mittal, T. (2022). Eruption chronology of the December 2021 to January 2022 Hunga Tonga-Hunga Ha'apai eruption sequence. *Communications Earth & Environment*, *3*. doi: 10.1038/s43247-022-00606-3

Hervig, M. E., & Deshler, T. (1998). Stratospheric aerosol surface area and volume inferred from HALOE, CLAES, and ILAS measurements. *J. Geophys. Res.*, *103*, 25,345–25,352. doi: 10.1029/98JD01962

Hofmann, D. J., & Solomon, S. (1989). Ozone destruction through heterogeneous chemistry following the eruption of El Chichòn. *J. Geophys. Res.*, *94*, 5029–5041.

Hunton, D. E., et al. (2005). In-situ aircraft observations of the 2000 Mt. Hekla volcanic cloud: Composition and chemical evolution in the Arctic lower stratosphere. *J. Vol. Geo. Res.*, *145*, 23–34. doi: 10.1016/j.jvolgeores.2005.01.005

Jenkins, S., Smith, C., Allen, M., & Grainger, R. (2023). Tonga eruption increases chance of temporary surface temperature anomaly above 1.5°C. *Nature Clim. Change*. doi: 10.1038/s41558-022-01568-2

Jurkat, T., Voigt, C., Arnold, F., Schlager, H., Aufmhoff, H., Schmale, J., ... Dörnbrack, A. (2010). Airborne stratospheric ITCIMS measurements of SO_2, HCl, and HNO_3 in the aged plume of volcano Kasatochi. *J. Geophys. Res.*, *115*. doi: 10.1029/2010JD013890

Keim, E. R., et al. (1996). Observations of large reductions in the NO/NO_y ratio near the mid-latitude tropopause and the role of heterogeneous chemistry. *Geophys. Res. Lett.*, *23*, 3223-3226. doi: 10.1029/96GL02593

Khaykin, S. M., et al. (2022). Global perturbation of stratospheric water and aerosol burden by Hunga eruption. *Communications Earth & Environment*, *3*. doi: 10.1038/s43247-022-00652-x

Kilian, M., Brinkop, S., & Jöckel, P. (2020). Impact of the eruption of Mt Pinatubo on the chemical composition of the stratosphere. *Atmos. Chem. Phys.*, *20*, 11697–11715. doi: 10.5194/acp-20-11697-2020

Kinnison, D. E., Grant, K. E., Connell, P. S., Rotman, D. A., & Wuebbles, D. J. (1994). The chemical and radiative effects of the Mount Pinatubo eruption. *J. Geophys. Res.*, *99*, 25,705–25,731.

Klobas, J. E., Wilmouth, D. M., Weisenstein, D. K., Anderson, J. G., & Salawitch, R. J. (2017). Ozone depletion following future volcanic eruptions. *Geophys. Res. Lett.*, *44*, 7490–7499. doi: 10.1002/2017GL073972

Koike, M., Jones, N. B., Matthews, W. A., Johnston, P. V., McKenzie, R. L., Kinnison, D., & Rodriguez, J. (1994). Impact of Pinatubo aerosols on the partitioning between NO_2 and HNO_3. *Geophys. Res. Lett.*, *21*, 597–600.

Kovilakam, M., & Deshler, T. (2015). On the accuracy of stratospheric aerosol extinction derived from in situ size distribution measurements and surface area density derived from remote SAGE II and HALOE extinction measurements. *J. Geophys. Res. Atmos.*, *120*, 8426–8447. doi: 10.1002/2015JD023303

Kumer, J. B., et al. (1996). Comparison of correlative data with HNO_3 version 7 from the CLAES instrument deployed on the NASA Upper Atmosphere Research Satellite. *J. Geophys. Res.*, *101*, 9621–9656.

Lambert, A., Livesey, N., & Read, W. (2020). *MLS/Aura Level 2 nitrous oxide (N2O) mixing ratio V005, Greenbelt, MD, USA, Goddard Earth Sciences Data and Information Services Center (GES DISC)* [dataset]. doi: https://doi.org/10.5067/Aura/MLS/DATA2515

Lambert, A., Read, W., & Livesey, N. (2020). *MLS/Aura Level 2 water vapor (H2O) mixing ratio V005, Greenbelt, MD, USA, Goddard Earth Sciences Data and Information Services Center (GES DISC)* [dataset]. doi: https://doi.org/10.5067/Aura/MLS/DATA2508

Lawrence, Z. D., Manney, G. L., & Wargan, K. (2018). Reanalysis intercomparisons of stratospheric polar processing diagnostics. *Atmos. Chem. Phys.*, *18*, 13547–13579. doi: 10.5194/acp-18-13547-2018

Legras, B., Duchamp, C., Sellitto, P., Podglajen, A., Carboni, E., Siddans, R., ... Ploeger, F. (2022). The evolution and dynamics of the Hunga Tonga–Hunga Ha'apai sulfate aerosol plume in the stratosphere. *Atmos. Chem. Phys.*, *22*, 14957–14970. doi: 10.5194/acp-22-14957-2022

Livesey, N. J., et al. (2020). *Version 5.0x Level 2 and 3 data quality and description document* (Tech. Rep. No. JPL D-105336 Rev. A). Pasadena: Jet Propulsion Laboratory. (Available at http://mls.jpl.nasa.gov.)

Livesey, N. J., et al. (2021). Investigation and amelioration of long-term instrumental drifts in water vapor and nitrous oxide measurements from the Aura Microwave Limb Sounder (MLS) and their implications for studies of variability and trends. *Atmos. Chem. Phys.*, *21*, 15409–15430. doi: 10.5194/acp-21-15409-2021

Mankin, W. G., Coffey, M. T., & Goldman, A. (1992). Airborne observations of SO_2, HCl and O_3 in the stratospheric plume of the Pinatubo volcano in July 1991. *Geophys. Res. Lett.*, *19*, 179–182.

Manney, G. L., & Millán, L. F. (2007–present). *Derived meteorological products for Aura Microwave Limb Sounder and other satellite datasets.* Retrieved from `https://mls.jpl.nasa.gov/eos-aura-mls/dmp` (Sign in required)

Manney, G. L., et al. (2023). Siege of the south: Hunga Tonga-Hunga Ha'apai water vapor excluded from 2022 Antarctic stratospheric polar vortex. *Geophys. Res. Lett.*. doi: 10.22541/essoar.168057560.00140372/v1

Manney, G. L., Santee, M., Froidevaux, L., Livesey, N., & Read, W. (2020). *MLS/Aura Level 2 nitric acid (HNO3) mixing ratio V005, Greenbelt, MD, USA, Goddard Earth Sciences Data and Information Services Center (GES DISC)* [dataset]. doi: https://doi.org/10.5067/Aura/MLS/DATA2511

Mather, T. A., Allen, A. G., Davison, B. M., Pyle, D. M., Oppenheimer, C., & McGonigle, A. J. S. (2004). Nitric acid from volcanoes. *Earth Planet. Sci. Lett.*, *218*, 17–30. doi: 10.1016/S0012-821X(03)00640-X

Mickley, L. J., Abbatt, J. P. D., Frederick, J. E., & Russell, J. M. (1997). Response of summertime odd nitrogen and ozone at 17 mbar to Mount Pinatubo aerosol over the southern midlatitudes: Observations from the Halogen Occultation Experiment. *J. Geophys. Res.*, *102*, 23,573–23,582.

Millán, L. F., et al. (2022). The Hunga Tonga-Hunga Ha'apai hydration of the stratosphere. *Geophys. Res. Lett.*, *49*. doi: 10.1029/2022GL099381

Millard, G. A., Mather, T. A., Pyle, D. M., Rose, W. I., & Thornton, B. (2006). Halogen emissions from a small volcanic eruption: Modeling the peak concentrations, dispersion, and volcanically induced ozone loss in the stratosphere. *Geophys. Res. Lett.*, *33*. doi: 10.1029/2006GL026959

Mills, M. J., Langford, A. O., O'Leary, T. J., Arpag, K., Miller, H. L., Proffitt, M. H., ... Solomon, S. (1993). On the relationship between stratospheric aerosols and nitrogen dioxide. *Geophys. Res. Lett.*, *20*, 1187–1190.

Naik, V., Horowitz, L. W., Schwarzkopf, M. D., & Lin, M. (2017). Impact of volcanic aerosols on stratospheric ozone recovery. *J. Geophys. Res. Atmos.*, *122*, 9515–9528. doi: 10.1002/2016JD025808

Oppenheimer, C., et al. (2010). Atmospheric chemistry of an Antarctic volcanic plume. *J. Geophys. Res.*, *115*. doi: 10.1029/2009JD011910

Poli, P., & Shapiro, N. M. (2022). Rapid characterization of large volcanic eruptions: Measuring the impulse of the Hunga Tonga Ha'apai explosion from teleseismic waves. *Geophys. Res. Lett.*, *49*. doi: 10.1029/2022GL098123

Prata, A. J., Carn, S. A., Stohl, A., & Kerkmann, J. (2007). Long range transport and fate of a stratospheric volcanic cloud from Soufrière Hills volcano, Montserrat. *Atmos. Chem. Phys.*, *7*, 5093–5103. doi: 10.5194/acp-7-5093-2007

Randel, W., Wu, F., Russell, J. M., Waters, J. W., & Froidevaux, L. (1995). Ozone and temperature changes in the stratosphere following the eruption of Mount Pinatubo. *J. Geophys. Res.*, *100*, 16,753–16,764.

Rieger, L. A., Randel, W. J., Bourassa, A. E., & Solomon, S. (2021). Stratospheric temperature and ozone anomalies associated with the 2020 Australian New Year fires. *Geophys. Res. Lett.*, *48*, e2021GL095898. doi: 10.1029/2021GL095898

Rinsland, C. P., Gunson, M. R., Abrams, M. C., Lowes, L. L., Zander, R., Mahieu, E., ... Sze, N. D. (1994). Heterogeneous conversion of N_2O_5 to HNO_3 in the post-Mount Pinatubo eruption stratosphere. *J. Geophys. Res.*, *99*, 8213–8219.

Rinsland, C. P., Weisenstein, D. K., Ko, M. K. W., Scott, C. J., Chiou, L. S., Mahieu, E., ... Demoulin, P. (2003). Post-Mount Pinatubo eruption ground-based infrared stratospheric column measurements of HNO_3, NO, and NO_2 and their comparison with model calculations. *J. Geophys. Res.*, *108*(D15),

4437. doi: 10.1029/2002JD002965

Robrecht, S., Vogel, B., Grooß, J.-U., Rosenlof, K., Thornberry, T., Rollins, A., ... Müller, R. (2019). Mechanism of ozone loss under enhanced water vapour conditions in the mid-latitude lower stratosphere in summer. *Atmos. Chem. Phys.*, *19*, 5805–5833. doi: 10.5194/acp-19-5805-2019

Rose, W. I., et al. (2006). Atmospheric chemistry of a 33-34 hour old volcanic cloud from Hekla volcano (Iceland): Insights from direct sampling and the application of chemical box modeling. *J. Geophys. Res.*, *111*. doi: 10.1029/2005JD006872

Santee, M. L., Livesey, N., & Read, W. (2020). *MLS/Aura Level 2 chlorine monoxide (ClO) mixing ratio V005, Greenbelt, MD, USA, Goddard Earth Sciences Data and Information Services Center (GES DISC)* [dataset]. doi: https://doi.org/10.5067/Aura/MLS/DATA2505

Santee, M. L., Manney, G. L., Livesey, N. J., & Read, W. G. (2004). Three-dimensional structure and evolution of stratospheric HNO_3 based on UARS Microwave Limb Sounder measurements. *J. Geophys. Res.*, *109*. doi: 10.1029/2004JD004578

Santee, M. L., et al. (2022). Prolonged and pervasive perturbations in the composition of the Southern Hemisphere midlatitude lower stratosphere from the Australian New Year's Fires. *Geophys. Res. Lett.*, *49*. doi: 10.1029/2021GL096270

Schoeberl, M. R., Wang, Y., Ueyama, R., Taha, G., Jensen, E., & Yu, W. (2022). Analysis and impact of the Hunga Tonga-Hunga Ha'apai stratospheric water vapor plume. *Geophys. Res. Lett.*, *49*. doi: 10.1029/2022GL100248

Schoeberl, M. R., Wang, Y., Ueyama, R., Taha, G., & Yu, W. (2023). The cross equatorial transport of the Hunga Tonga-Hunga Ha'apai eruption plume. *Geophys. Res. Lett.*, *50*. doi: 10.1029/2022GL102443

Schwartz, M., Froidevaux, L., Livesey, N., & Read, W. (2020). *MLS/Aura Level 2 ozone (O3) mixing ratio V005, Greenbelt, MD, USA, Goddard Earth Sciences Data and Information Services Center (GES DISC)* [dataset]. doi: https://doi.org/10.5067/Aura/MLS/DATA2506

Sellitto, P., et al. (2022). The unexpected radiative impact of the Hunga Tonga eruption of 15th January 2022. *Communications Earth & Environment*, *3*. doi: 10.1038/s43247-022-00618-z

Sheese, P. E., Boone, C. D., & Walker, K. A. (2015). Detecting physically unrealistic outliers in ACE-FTS atmospheric measurements. *Atmos. Meas. Tech.*, *8*, 741–750. doi: 10.5194/amt-8-741-2015

Sheese, P. E., & Walker, K. A. (2020). *Data Quality Flags for ACE-FTS Level 2 Version 4.1 Data Set* [dataset]. Retrieved from `https://doi.org/10.5683/SP2/BC4ATC` doi: 10.5683/SP2/BC4ATC

Slusser, J., Liu, X., Stamnes, K., Shaw, G., Smith, R., Storvold, R., ... Good, P. (1998). High-latitude stratospheric NO_2 and HNO_3 over Fairbanks (65°N) 1992–1994. *J. Geophys. Res.*, *103*, 1549–1554.

Solomon, S. (1999). Stratospheric ozone depletion: A review of concepts and history. *Rev. Geophys.*, *37*, 275–316.

Solomon, S., Ivy, D. J., Kinnison, D., Mills, M. J., Neely III, R. R., & Schmidt, A. (2016). Emergence of healing in the Antarctic ozone layer. *Science*, *353*, 269–274. doi: 10.1126/science.aae0061

Solomon, S., et al. (2022). On the stratospheric chemistry of midlatitude wildfire smoke. *Proc. Natl. Acad. Sci. U.S.A.*, *119*. doi: 10.1073/pnas.2117325119

Solomon, S., Stone, K., Yu, P., Murphy, D. M., Kinnison, D., Ravishankara, A. R., & Wang, P. (2023). Chlorine activation and enhanced ozone depletion induced by wildfire aerosol. *Nature*, *615*, 259–264. doi: 10.1038/s41586-022-05683-0

Stone, K., et al. (2017). Observing the impact of Calbuco volcanic aerosols on South Polar ozone depletion in 2015. *J. Geophys. Res. Atmos.*, *122*, 11,862–11,879.

doi: 10.1002/2017JD026987

Strahan, S. E., Douglass, A. R., Newman, P. A., & Steenrod, S. D. (2014). Inorganic chlorine variability in the Antarctic vortex and implications for ozone recovery. *J. Geophys. Res. Atmos.*, *119*, 14,098–14,109. doi: 10.1002/2014JD022295

Strahan, S. E., et al. (2022). Unexpected repartitioning of stratospheric inorganic chlorine after the 2020 Australian wildfires. *Geophys. Res. Lett.*, *49*. doi: 10.1029/2022GL098290

Tabazadeh, A., & Turco, R. P. (1993). Stratospheric chlorine injection by volcanic eruptions: HCl scavenging and implications for ozone. *Science*, *260*, 1082–1085.

Taha, G. (2020). *OMPS-NPP L2 LP aerosol extinction vertical profile swath daily 3slit V2* [dataset]. Retrieved from `https://doi.org/10.5067/CX2B9NW6FI27` doi: 10.5067/CX2B9NW6FI27

Taha, G., Loughman, R., Colarco, P. R., Zhu, T., Thomason, L. W., & Jaross, G. (2022). Tracking the 2022 Hunga Tonga-Hunga Ha'apai aerosol cloud in the upper and middle stratosphere using space-based observations. *Geophys. Res. Lett.*, *49*. doi: 10.1029/2022GL100091

Taha, G., Loughman, R., Zhu, T., Thomason, L., Kar, J., Rieger, L., & Bourassa, A. (2021). OMPS LP Version 2.0 multi-wavelength aerosol extinction coefficient retrieval algorithm. *Atmos. Meas. Tech.*, *14*, 1015–1036. doi: 10.5194/amt-14-1015-2021

Textor, C., Graf, H.-F., Herzog, M., & Oberhuber, J. M. (2003). Injection of gases into the stratosphere by explosive volcanic eruptions. *J. Geophys. Res.*, *108*(D19), 4606. doi: 10.1029/2002JD002987

Theys, N., Smedt, I. D., Roozendael, M. V., Froidevaux, L., Clarisse, L., & Hendrick, F. (2014). First satellite detection of volcanic OClO after the eruption of Puyehue-Cordón Caulle. *Geophys. Res. Lett.*, *41*, 667–672. doi: 10.1002/2013GL058416

Tie, X., Brasseur, G. P., Briegleb, B., & Granier, C. (1994). Two-dimensional simulation of Pinatubo aerosol and its effect on stratospheric ozone. *J. Geophys. Res.*, *99*, 20,545–20,562,.

Toohey, D. W., Avallone, L. M., Lait, L. R., Newman, P. A., Schoeberl, M. R., Fahey, D. W., ... Anderson, J. G. (1993). The seasonal evolution of reactive chlorine in the northern hemisphere stratosphere. *Science*, *261*, 1134–1136. doi: 10.1126/science.261.5125.1134

Voigt, C., Jessberger, P., Jurkat, T., Kaufmann, S., Baumann, R., Schlager, H., ... Salerno, G. (2014). Evolution of CO_2, SO_2, HCl, and HNO_3 in the volcanic plumes from Etna. *Geophys. Res. Lett.*, *41*, 2196–2203. doi: 10.1002/2013GL058974

Vömel, H., Evan, S., & Tully, M. (2022). Water vapor injection into the stratosphere by Hunga Tonga-Hunga Ha'apai. *Science*, *377*, 1444–1447. doi: 10.1126/science.abq2299

Wallace, L., & Livingston, W. (1992). The effect of the Pinatubo cloud on hydrogen chloride and hydrogen fluoride. *Geophys. Res. Lett.*, *19*, 1209. doi: 10.1029/92GL01112

Wang, S., Pickett, H., Livesey, N., & Read, W. (2020). *MLS/Aura Level 2 hydroperoxy (HO2) mixing ratio V005, Greenbelt, MD, USA, Goddard Earth Sciences Data and Information Services Center (GES DISC)* [dataset]. doi: https://doi.org/10.5067/Aura/MLS/DATA2512

Waters, J. W., et al. (2006). The Earth Observing System Microwave Limb Sounder (EOS MLS) on the Aura satellite. *IEEE Trans. Geosci. Remote Sens.*, *44*, 1075–1092. doi: 10.1109/TGRS.2006.873771

Wilka, C., Shah, K., Stone, K., Solomon, S., Kinnison, D., Mills, M., ... Neely III, R R (2018). On the role of heterogeneous chemistry in ozone depletion and recovery. *Geophys. Res. Lett.*, *45*, 7835–7842. doi: 10.1029/2018GL078596

Wilson, J. C., et al. (1993). In situ observations of aerosol and chlorine monoxide after the 1991 eruption of Mount Pinatubo: Effect of reactions on sulfate aerosol. *Science*, *261*, 1140–1143. doi: 10.1126/science.261.5125.1140

Witze, A. (2022). Why the Tongan eruption will go down in the history of volcanology. *Nature*, *602*, 376–378. doi: 10.1038/d41586-022-00394-y

Wright, C. J., et al. (2022). Surface-to-space atmospheric waves from Hunga Tonga-Hunga Ha'apai eruption. *Nature*, *609*, 741–746. doi: 10.1038/s41586-022-05012-5

Xu, J., Li, D., Bai, Z., Tao, M., & Bian, J. (2022). Large amounts of water vapor were injected into the stratosphere by the Hunga Tonga-Hunga Ha'apai volcano eruption. *Atmosphere*, *13*. doi: 10.3390/atmos13060912

Yu, P., Davis, S. M., Toon, O. B., Portmann, R. W., Bardeen, C. G., Barnes, J. E., et al. (2021). Persistent stratospheric warming due to 2019–2020 Australian wildfire smoke. *Geophys. Res. Lett.*, *48*. doi: 10.1029/2021GL092609

Yuen, D. A., et al. (2022). Under the surface: Pressure-induced planetary-scale waves, volcanic lightning, and gaseous clouds caused by the submarine eruption of Hunga Tonga-Hunga Ha'apai volcano. *Earthquake Res. Adv.*, *2*. doi: 10.1016/j.eqrea.2022.100134

Zambri, B., Solomon, S., Kinnison, D. E., Mills, M. J., Schmidt, A., Neely III, R R, ... Roth, C. Z. (2019). Modeled and observed volcanic aerosol control on stratospheric NO_y and Cl_y. *J. Geophys. Res. Atmos.*, *124*, 10,283–10,303. doi: 10.1029/2019JD031111

Zhu, Y., et al. (2022). Perturbations in stratospheric aerosol evolution due to the water-rich plume of the 2022 Hunga-Tonga eruption. *Communications Earth & Environment*, *3*. doi: 10.1038/s43247-022-00580-w

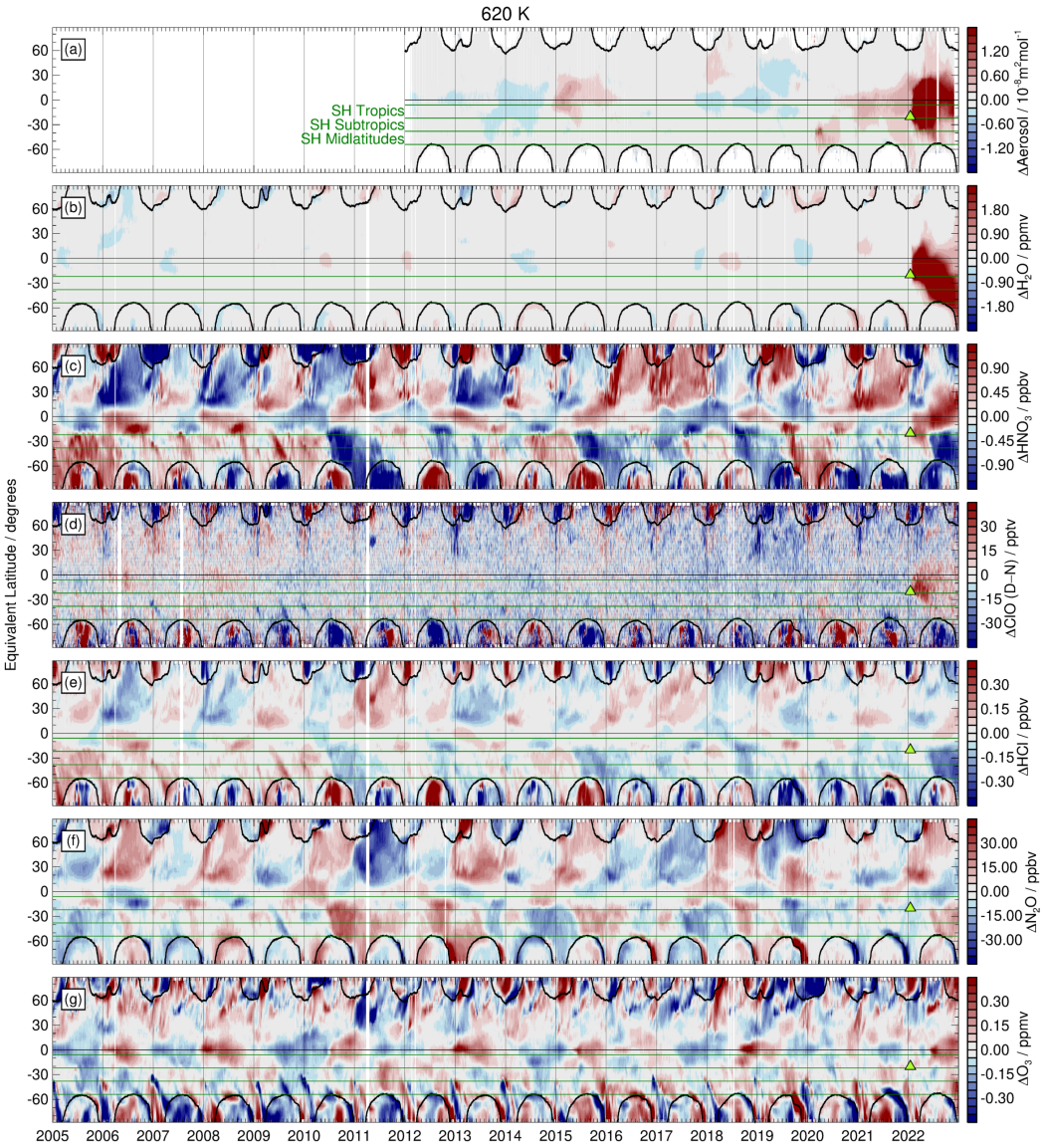

Figure 1. Equivalent latitude (EqL) / time series at 620 K of anomalies (calculated by subtracting from the daily data in each EqL bin the corresponding climatological value over 2005–2021 for MLS and 2012–2021 for OMPS-LP for that day of the year) in (a) NASA OMPS-LP aerosol cross section at 869 nm and MLS (b) H_2O, (c) HNO_3, (d) ClO (day minus night), (e) HCl, (f) N_2O, and (g) O_3. To ameliorate a negative drift in the MLS N_2O measurements (see Section 2), the N_2O anomalies (panel (f)) have been "detrended" by removing a linear fit to the daily values across the Aura mission at each EqL/potential temperature gridpoint. Blank spaces represent data gaps. Black overlays identify the approximate boundary of the winter polar vortices (as defined by Lawrence et al., 2018). The black horizontal line marks the equator; green horizontal lines mark the EqLs defining the regions examined in this study: the southern tropics (6°S–22°S), subtropics (22°S–38°S), and midlatitudes (38°S–54°S). The bright green triangle marks the time and latitude of the main HT-HH eruption.

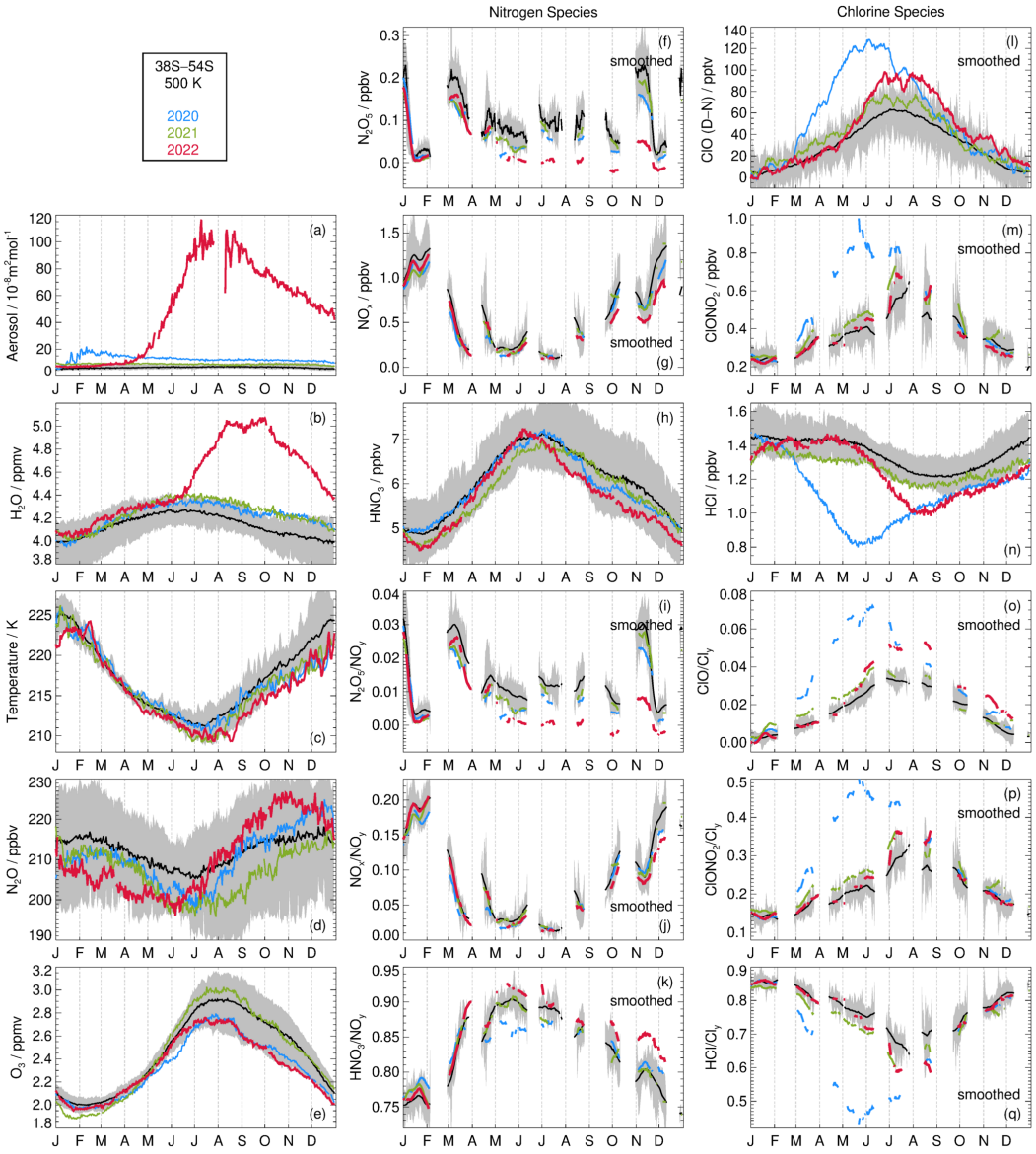

Figure 2. Averages over 38°S–54°S EqL (southern midlatitudes) at 500 K of (a) NASA OMPS-LP aerosol cross section at 869 nm, (b) MLS H_2O, (c) MERRA-2 temperature, (d) MLS N_2O, (e) MLS O_3, (f) ACE-FTS N_2O_5, (g) ACE-FTS NO_x ($NO+NO_2$), (h) MLS HNO_3, (i) N_2O_5/NO_y (where $NO_y=N_2O_5+NO_x+HNO_3+ClONO_2$), (j) NO_x/NO_y, (k) HNO_3/NO_y, (l) MLS ClO (day minus night), (m) ACE-FTS $ClONO_2$, (n) MLS HCl, (o) ClO/Cl_y (where $Cl_y=ClO+ClONO_2+HCl$), (p) $ClONO_2/Cl_y$, and (q) HCl/Cl_y. Values for 2022 are shown in red, for 2021 in green, and for 2020 in blue. Grey shading depicts the envelope of behavior and black lines the mean over 2005–2019 (thus excluding the highlighted years). ClO is one of the noisier MLS products; in addition, for this analysis we are taking day minus night differences, so fewer individual points contribute to these EqL-band averages than for the other species measured by MLS. Consequently, the ClO field displays a fairly large degree of day-to-day variability. To enhance clarity, the ClO results (highlighted years and mean, but not the envelope) have been smoothed using a boxcar of width 10 days. Although such smoothing attenuates extreme values, it facilitates detection of persistent anomalies. Similarly, all ACE-FTS fields, as well as all quantities derived using them, have also been smoothed with a 10-day boxcar average.

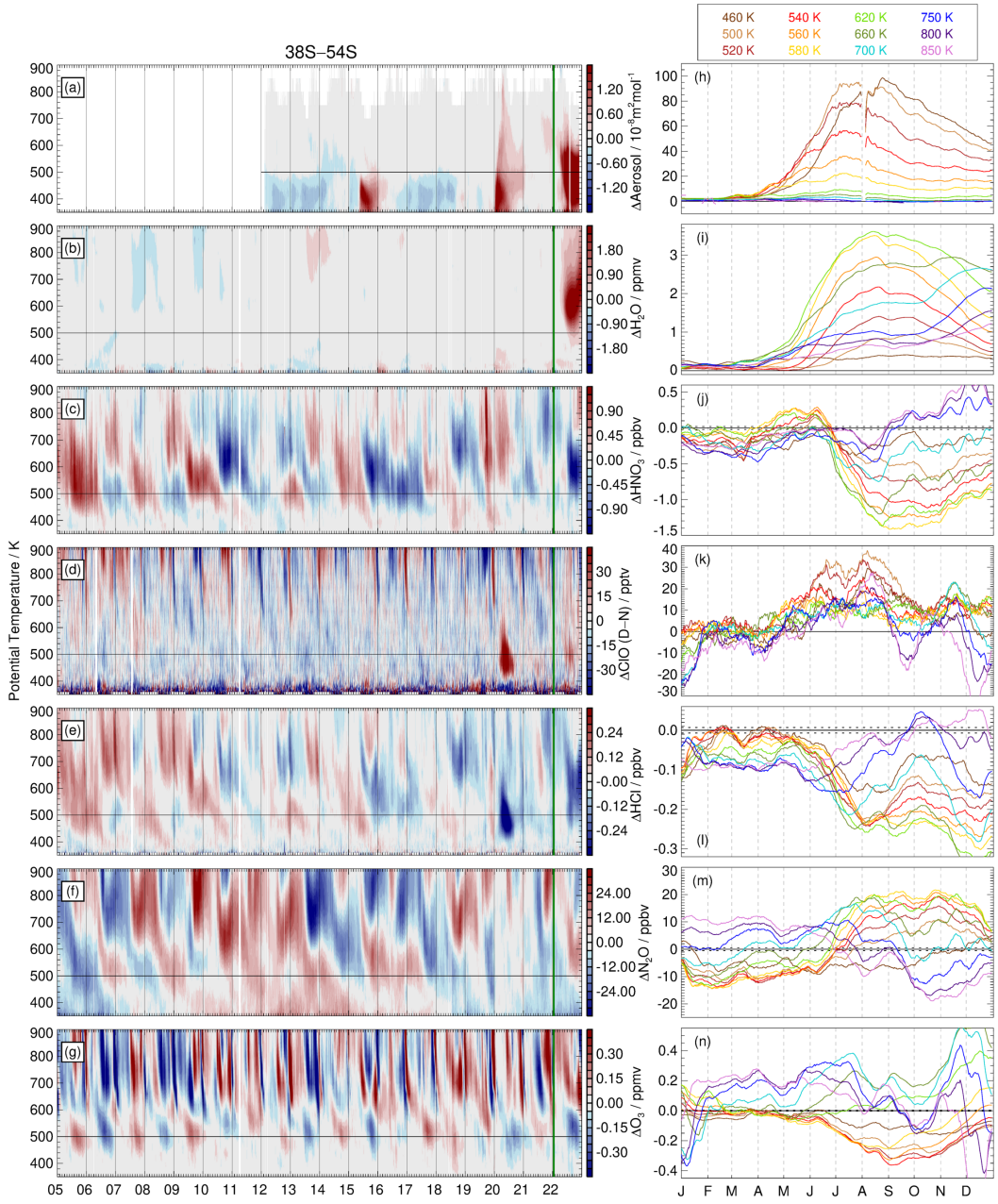

Figure 3. Potential temperature / time sections of anomalies (calculated as in Figure 1) in the 38°S–54°S EqL band of (a) NASA OMPS-LP aerosol cross section at 869 nm and MLS (b) H_2O, (c) HNO_3, (d) ClO (day minus night), (e) HCl, (f) N_2O, and (g) O_3. The vertical green line marks the date of the main HT-HH eruption. Panels (h)–(n) show the 2022 anomalies for each species at multiple potential temperatures (see legend). To enhance clarity, all curves in (h)–(n) except ClO have been smoothed using a boxcar of width 10 days; for ClO the smoothing window is 20 days. This smoothing removes some of the small-scale structure seen in the unsmoothed EqL-band averages shown in Figure 2. Solid black horizontal lines mark zero. Dashed black horizontal lines on the bottom five panels denote the 2σ contributions ($\pm$ values) of MLS measurement noise to the smoothed EqL-band average anomalies, taken to indicate likely statistical significance for individual points in the anomaly timeseries.

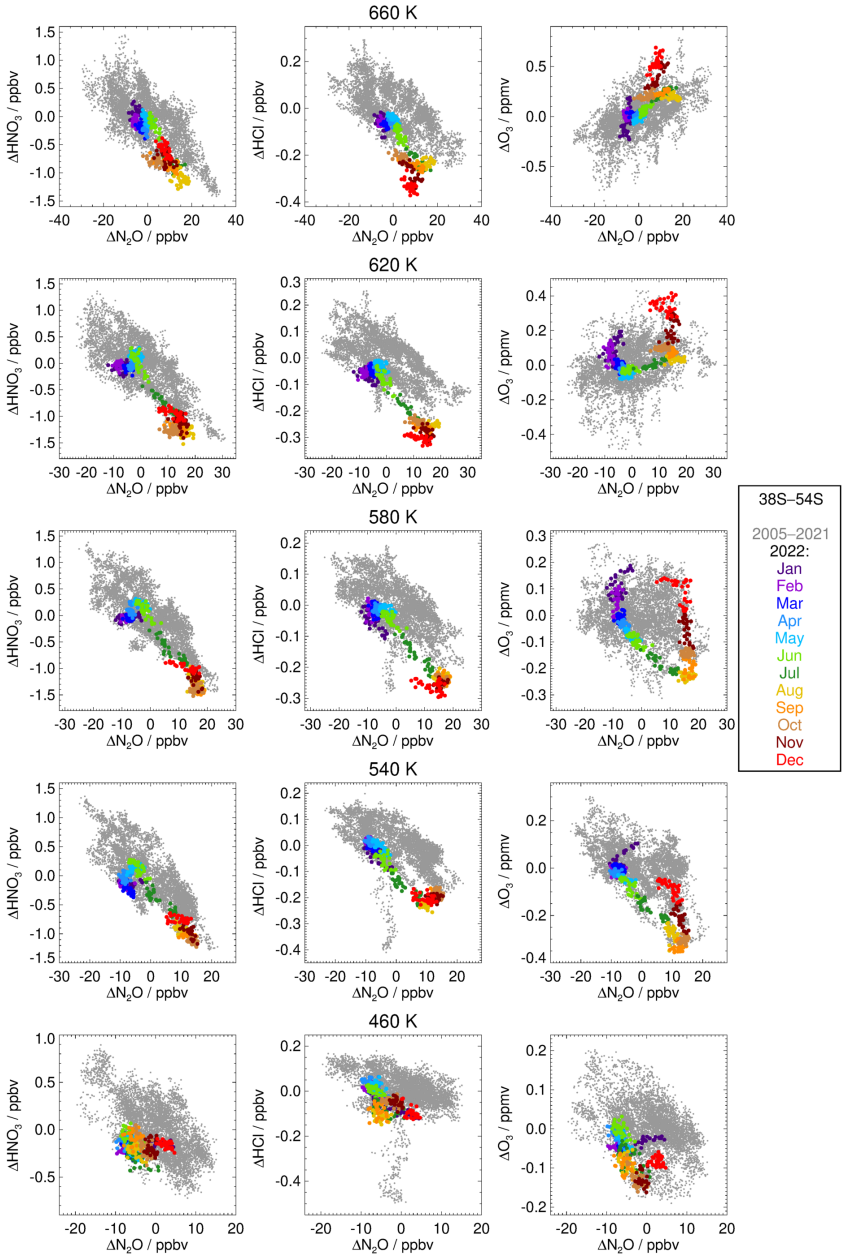

Figure 4. Scatter plots of daily HNO_3 (left), HCl (middle), and O_3 (right) vs. N_2O anomalies in the 38°S–54°S EqL band at various potential temperature levels. Grey dots depict data from 2005–2021; 2022 data are color-coded by month (see legend).

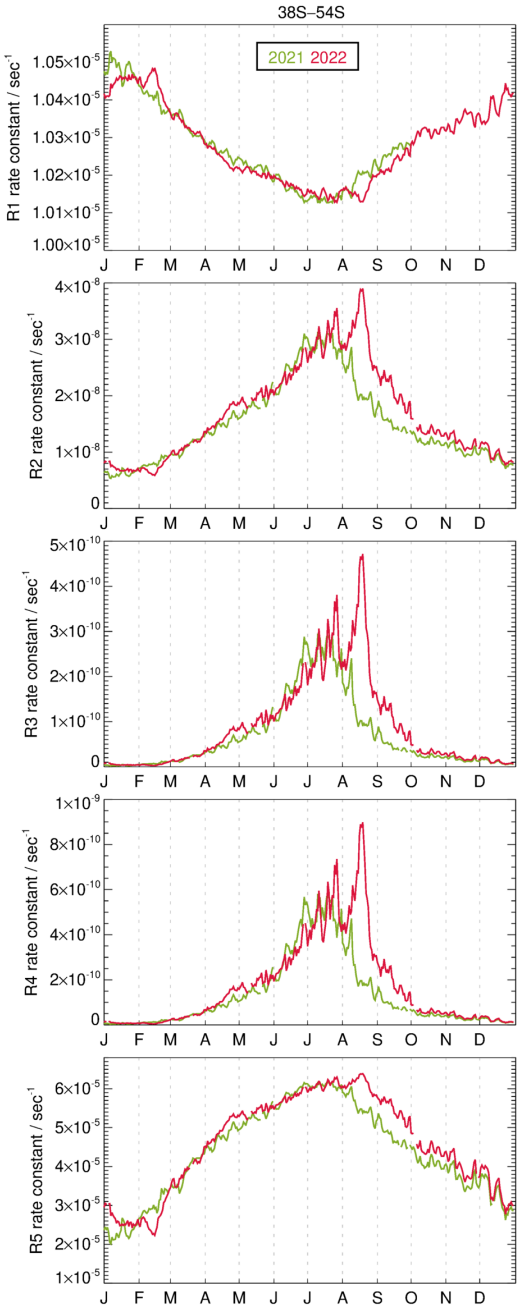

Figure 5. First-order rate constants for reactions R1–R5 in the 38°S–54°S EqL band at 500 K, based on the daily mean temperature and water vapor abundances observed in this region and the reactive uptake coefficients in Figure S1 in Supporting Information, assuming fixed abundances of 2 ppbv HCl, 0.1 ppbv $ClONO_2$, 0.1 ppbv HOCl, and 0.1 ppbv H_2SO_4 for a mean particle radius of 0.1μm and an SAD of 2 $\mu m^2\,cm^{-3}$. Values for 2022 are shown in red and for 2021 in green.

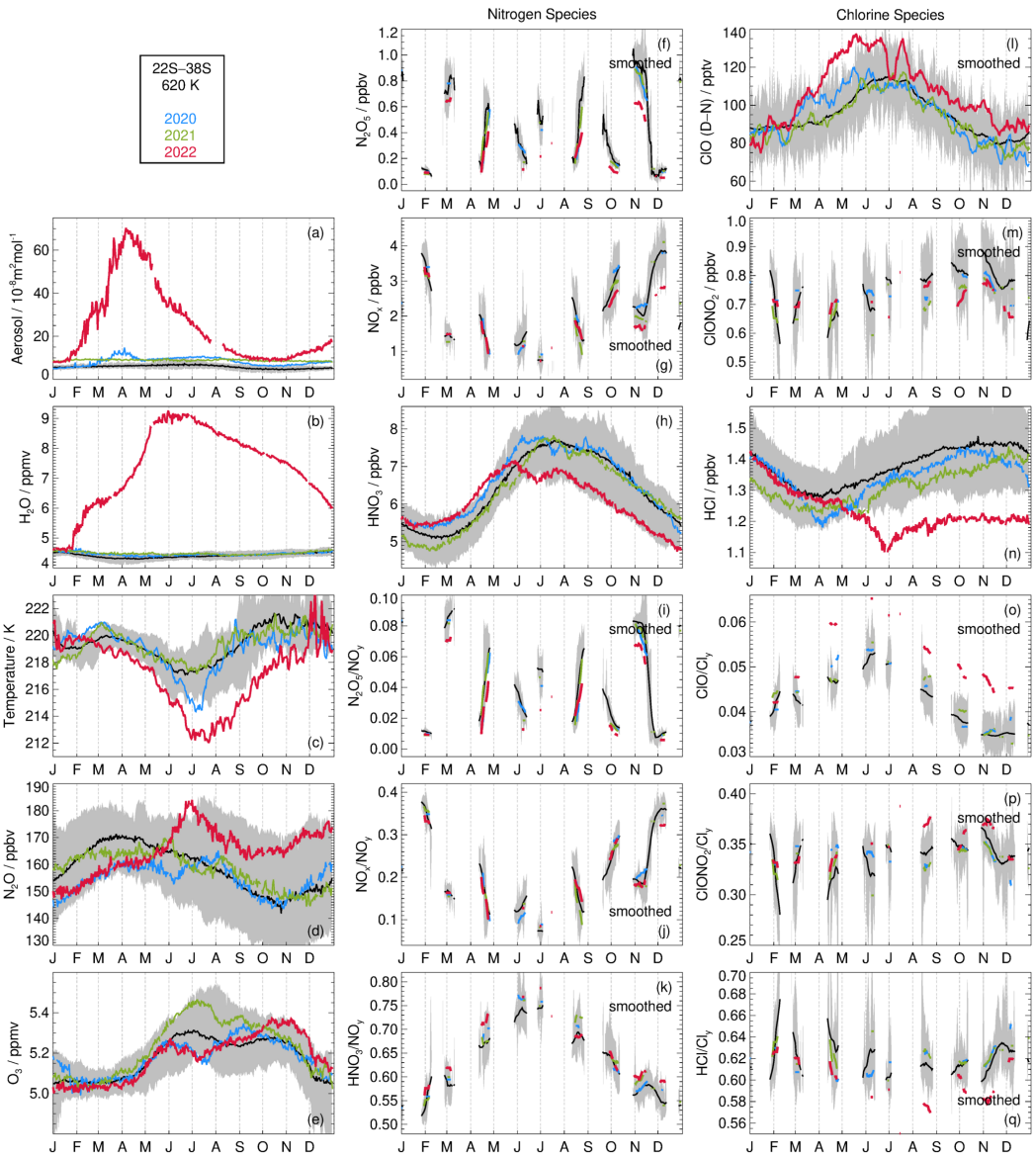

Figure 6. As Figure 2, but for 22°S–38°S EqL (southern subtropics) at 620 K.

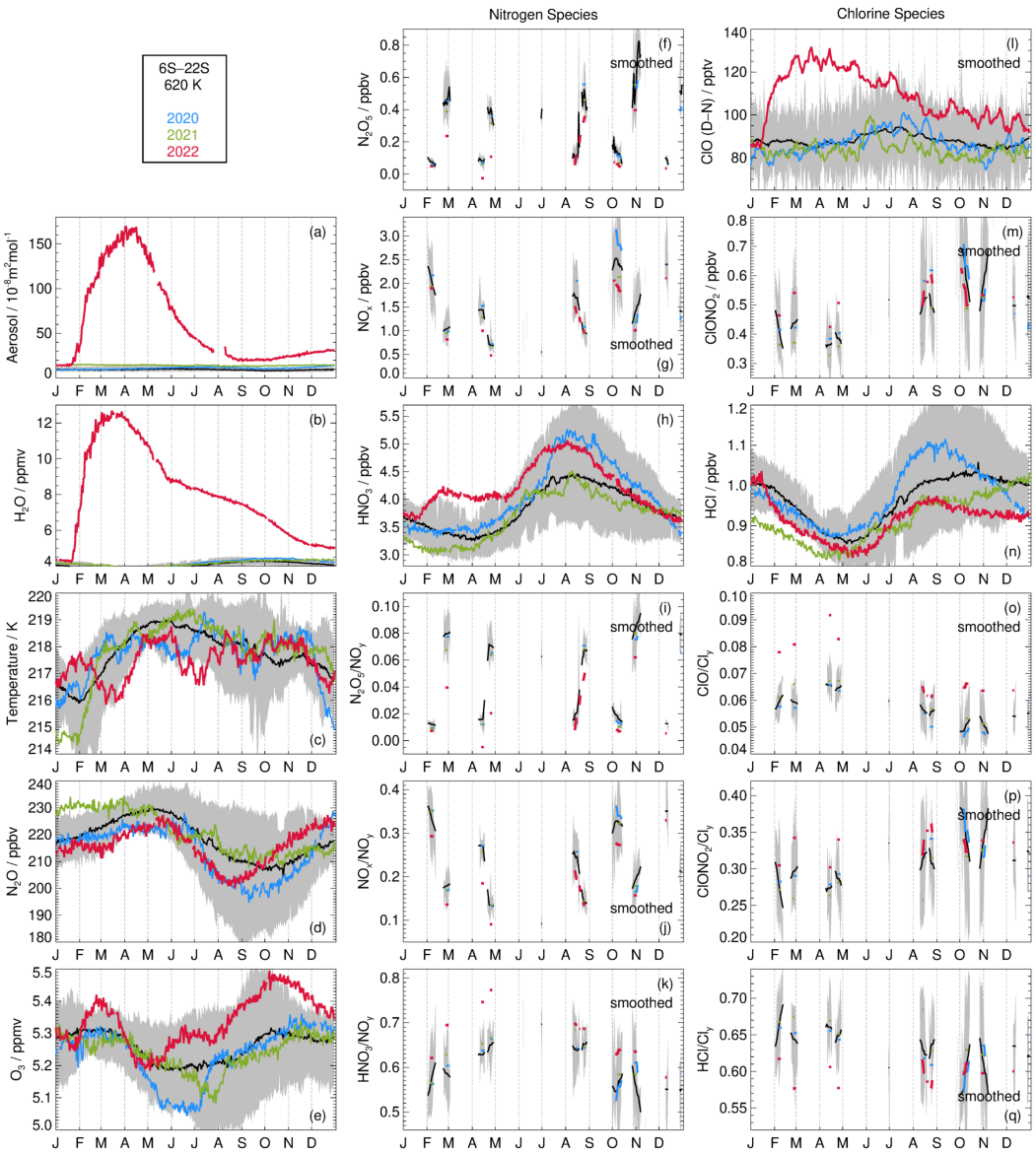

Figure 7. As Figure 2, but for 6°S–22°S EqL (southern tropics) at 620 K.

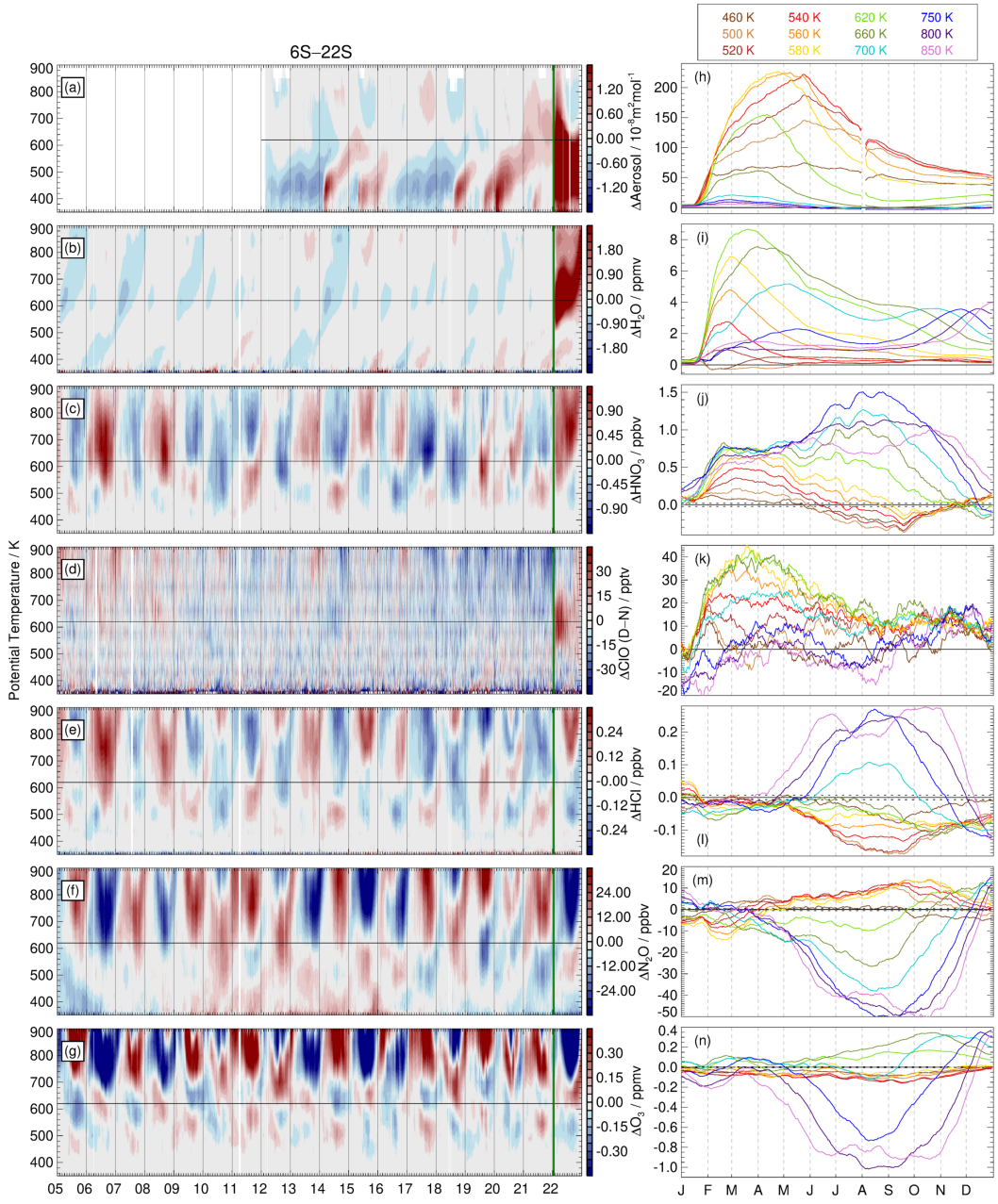

Figure 8. As Figure 3, but for 6°S–22°S EqL.

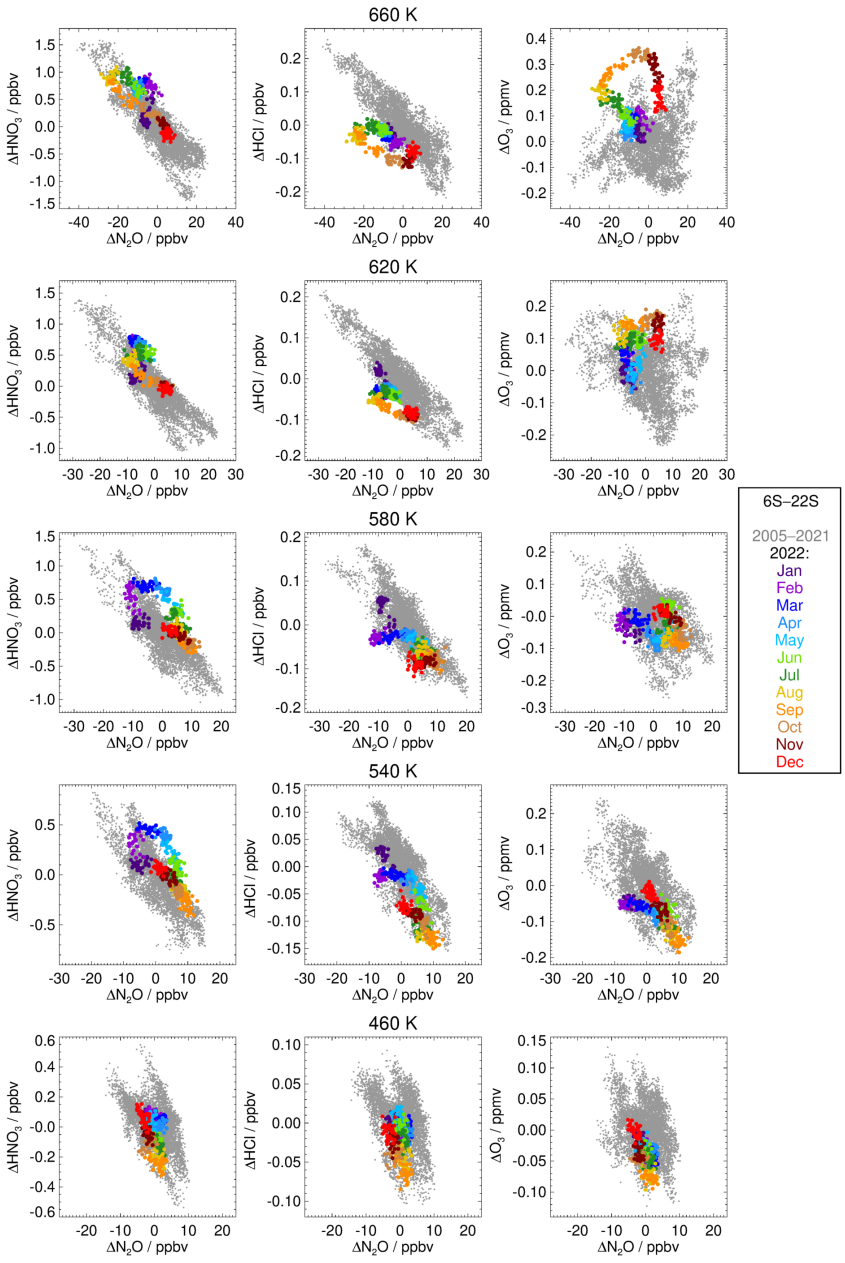

Figure 9. As Figure 4, but for 6°S–22°S EqL.

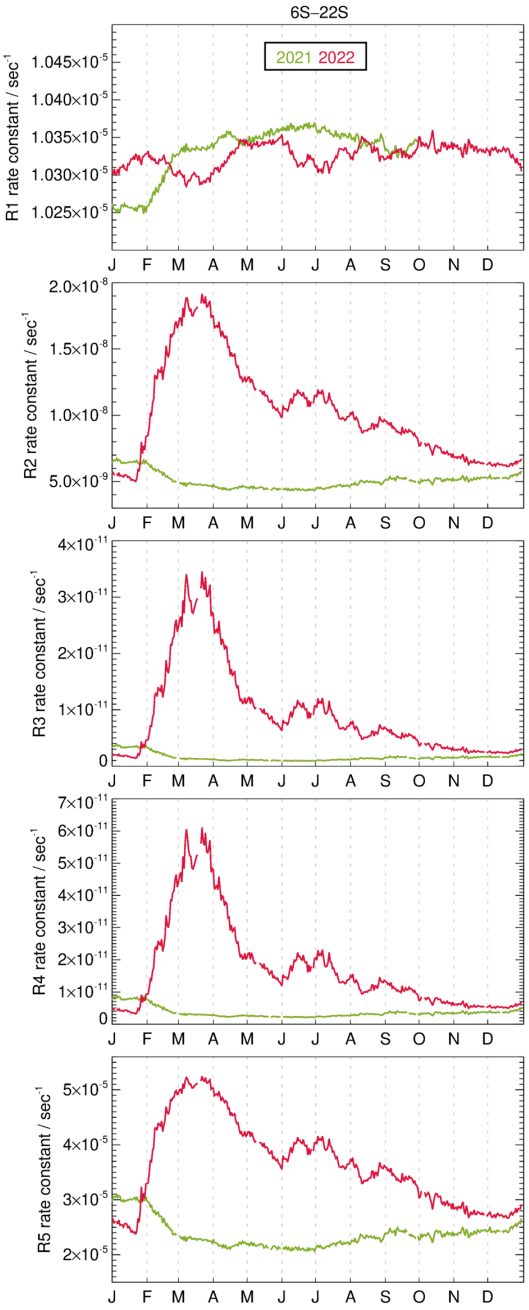

Figure 10. As Figure 5, but for 6°S–22°S EqL at 620 K.